



RESEARCH ARTICLE

10.1029/2021MS002902

Differences in Tropical Rainfall in Aquaplanet Simulations With Resolved or Parameterized Deep Convection

Rosimar Rios-Berrios¹ , George H. Bryan¹ , Brian Medeiros¹ , Falko Judt¹ , and Wei Wang¹¹National Center for Atmospheric Research, Boulder, CO, USA**Key Points:**

- Resolved deep convection yields more intense rainfall rates in the tropics—from the intertropical convergence zone to individual precipitation systems
- Equatorial waves appear at all horizontal resolutions, but their variability and intensity are stronger when deep convection is resolved
- Linear convective systems, resolved cold pools, and upgradient momentum fluxes explain the stronger rainfall with resolved convection

Supporting Information:

Supporting Information may be found in the online version of this article.

Correspondence to:R. Rios-Berrios,
rberrios@ucar.edu**Citation:**

Rios-Berrios, R., Bryan, G. H., Medeiros, B., Judt, F., & Wang, W. (2022). Differences in tropical rainfall in aquaplanet simulations with resolved or parameterized deep convection. *Journal of Advances in Modeling Earth Systems*, 14, e2021MS002902. <https://doi.org/10.1029/2021MS002902>

Received 10 NOV 2021

Accepted 21 APR 2022

Abstract This study investigates the effects of resolved deep convection on tropical rainfall and its multi-scale variability. A series of aquaplanet simulations are analyzed using the Model for Prediction Across Scales-Atmosphere with horizontal cell spacings from 120 to 3 km. The 3-km experiment uses a novel configuration with 3-km cell spacing between 20°S and 20°N and 15-km cell spacing poleward of 30°N/S. A comparison of those experiments shows that resolved deep convection yields a narrower, stronger, and more equatorward intertropical convergence zone, which is supported by stronger nonlinear horizontal momentum advection in the boundary layer. There is also twice as much tropical rainfall variance in the experiment with resolved deep convection than in the experiments with parameterized convection. All experiments show comparable precipitation variance associated with Kelvin waves; however, the experiment with resolved deep convection shows higher precipitation variance associated with westward propagating systems. Resolved deep convection also yields at least two orders of magnitude more frequent heavy rainfall rates ($>2 \text{ mm hr}^{-1}$) than the experiments with parameterized convection. A comparison of organized precipitation systems demonstrates that tropical convection organizes into linear systems that are associated with stronger and deeper cold pools and upgradient convective momentum fluxes when convection is resolved. In contrast, parameterized convection results in more circular systems, weaker cold pools, and downgradient convective momentum fluxes. These results suggest that simulations with parameterized convection are missing an important feedback loop between the mean state, convective organization, and meridional gradients of moisture and momentum.

Plain Language Summary Tall cumulonimbus clouds are abundant in the tropics. However, those clouds are so narrow and evolve so quickly that they cannot be captured by most weather prediction and climate models. Most of those models rely on a separate component, called a deep convection parameterization, to approximate the presence and evolution of cumulonimbus clouds and their associated processes. In this study, we use a specialized model that can use such a parameterization to approximate cumulonimbus clouds, or can explicitly produce those clouds without a parameterization given sufficient resolution. We then compare the characteristics of tropical weather systems from these two approaches. Our comparison shows that when the parameterization is used, the model produces lighter rainfall from circular clusters of clouds. Rainfall in these experiments happens only when there is enough water vapor and warming in the atmosphere to create clouds and rainfall. In contrast, when deep clouds are produced with fine resolution and no parameterization, the results are more realistic, with heavier rainfall organized into linear clusters of clouds. These results suggest that improvements to the representation of cumulonimbus clouds, either directly in the model or through improved parameterizations, would result in more accurate weather and climate predictions.

1. Motivation

Tropical rainfall systems happen across many spatiotemporal scales. On the planetary scale, clouds and rainfall organize along a narrow band known as the intertropical convergence zone (ITCZ). Within the ITCZ, zonally-propagating phenomena—known as convectively coupled equatorial waves—modulate tropical rainfall from days to weeks and from synoptic to planetary scales (Kiladis et al., 2009). Embedded within those waves are groups of organized precipitation systems known as mesoscale convective systems, which have a lifetime of hours to days but which contribute over 50% of the climatological rainfall in the tropics (Nesbitt et al., 2006). While most convective systems are organized into clusters, a large fraction of the total vertical mass flux is accomplished by relatively narrow, weak updrafts (Yuter & Houze, 1995; Zipser & LeMone, 1980). The objective of this paper is to examine how those multiscale processes are represented in global models when deep convection is explicitly resolved or parameterized.

© 2022 The Authors. Journal of Advances in Modeling Earth Systems published by Wiley Periodicals LLC on behalf of American Geophysical Union. This is an open access article under the terms of the [Creative Commons Attribution-NonCommercial-NoDerivs License](https://creativecommons.org/licenses/by/4.0/), which permits use and distribution in any medium, provided the original work is properly cited, the use is non-commercial and no modifications or adaptations are made.

Climate and weather prediction models exhibit some noteworthy deficiencies when tropical convection is parameterized. Some climate models simulate a double ITCZ instead of the expected single ITCZ in time-mean zonal-mean diagnostics of rainfall (Lin, 2007; Mechoso et al., 1995). Accurately capturing rainfall variability driven by convectively coupled equatorial waves is also a challenge for some models. For example, a comparison of 20 general circulation models against satellite observations found that only five models captured equatorial Kelvin waves reasonably well (Straub et al., 2010). Additionally, global models are unable to capture high-intensity precipitation events that often result in extreme precipitation and flooding hazards in the tropics (e.g., Haiden et al., 2012; Vogel et al., 2018). Most of the aforementioned deficiencies are hypothesized to stem from the convection parameterizations that are employed when the grid spacing is larger than roughly 10 km (Dias et al., 2018; Frierson, 2007; Frierson et al., 2011; Lin et al., 2006; Liu et al., 2010; Möbis & Stevens, 2012; Nakajima et al., 2013; Nolan et al., 2016; Pearson et al., 2014; Peatman et al., 2018; Seo et al., 2012; Straub et al., 2010).

That hypothesis has been investigated with global storm-resolving models—that is, models that use grid spacing smaller than 10 km and no convection parameterization (e.g., Becker et al., 2021; Hohenegger et al., 2020; Judt, 2018; Judt et al., 2021; Judt & Rios-Berrios, 2021; Stevens et al., 2019; Weber et al., 2020; Weber & Mass, 2019; Wedi et al., 2020). For example, Weber et al. (2020) and Judt and Rios-Berrios (2021) demonstrated that forecasts using resolved deep convection produced the most accurate rainfall variability associated with equatorial waves. Weber et al. (2020) attributed their results to a more accurate nonlinear moisture-rainfall relationship than when using a convection parameterization. Judt and Rios-Berrios (2021) further showed that the improved representation of rainfall variability stemmed from explicitly resolving convection because their simulations with sub 10 km cell spacing and a convection parameterization did not show improvements over the simulations with 15 km cell spacing or greater. Not all aspects of tropical rainfall are improved in global models with explicit convection; for instance, resolving convection can produce overly intense rainfall that precludes the formation of mesoscale convective systems (Becker et al., 2021; Stevens et al., 2019).

Finding solutions to improve the representation of tropical rainfall can be a challenge due to the complex interactions happening in global models. Idealized model simulations of Earth-like conditions, such as aquaplanet experiments, can reduce some of those complexities while still modeling physical processes in a realistic framework. Furthermore, an idealized configuration facilitates comparison across different models such as was done in the Aqua-Planet Experiment (APE, Blackburn & Hoskins, 2013). A comparison of 16 global models in APE showed a variety of solutions for the tropical atmosphere (Blackburn et al., 2013; Nakajima et al., 2013; Williamson et al., 2013). Some models exhibited a single ITCZ while other models developed double ITCZs for the same sea-surface temperature (SST) profile, but the solution changed for some models when the underlying SST profile was changed (Blackburn et al., 2013; Williamson et al., 2013). The models also exhibited quite the variety of propagating tropical waves; some models captured mostly eastward propagating features while other models captured westward or even stationary features (Nakajima et al., 2013). A more recent comparison of a smaller subset of models using the same configuration as in the APE showed similar intermodel spread (Rios-Berrios et al., 2020a, 2020b), suggesting that clearly more research is still needed to better understand and simulate the dynamics of the tropical atmosphere.

Aquaplanet experiments using the same model with different horizontal resolution allow exploring the benefits of resolved deep convection in comparison to parameterized convection. Tomita (2005) produced one of the first aquaplanet simulations with explicitly resolved convection (mesh spacing of 3.5, 7 and 14 km), demonstrating that the sub 10 km simulations captured many realistic tropical phenomena such as equatorial waves. Nasuno et al. (2007) examined the simulations of Tomita (2005) in more detail, finding that the realistic representation of equatorial waves was, in part, due to a realistic representation of cloud clusters ranging from synoptic to convective scales. Nasuno et al. (2007) further showed that mesoscale cloud clusters were maintained by convective elements organized along the leading edges of cold pools. While those simulations were insightful, the 3.5 km simulation was only integrated for 10 days due to computational constraints at the time. Nolan et al. (2016) presented longer convection-permitting simulations except with an “aquapatch”, which used a limited-area beta-plane representative of one third the length of the equator. Interestingly, Nolan et al. (2016) also suggested that resolved cold pools were important, except they argue that cold pools redistributed precipitation away from the equator resulting in a single, weak ITCZ when the grid spacing was reduced to 5 km. In contrast, Retsch et al. (2019) found a double ITCZ in aquaplanet simulations with convection-permitting resolution although with

Table 1
Summary of the Aquaplanet Experiments Analyzed in This Study

Simulation name	Horizontal cell spacing	Diffusion length scale	Time step	Simulation length
120 km	120 km everywhere	120 km	720 s	791 days
30 km	30 km everywhere	30 km	180 s	791 days
15 km	15 km everywhere	15 km	90 s	791 days
3 km	3 km between 20°S and 20°N, 15 km poleward of 30°N/S	3 km	15 s	160 days

a different modeling system. It appears that the presence of a single or double ITCZ may depend on factors other than explicitly resolving convection.

Longer simulations with a more diverse range of model configurations are necessary to further identify potential benefits of explicitly resolved convection, which in turn could potentially inform the improvement of convection parameterizations. To this end, the primary purpose of this manuscript is to investigate differences of simulated tropical rainfall in relatively long aquaplanet experiments when deep convection is either parameterized (using relatively large grid spacing) or explicitly resolved (with relatively small grid spacing). We describe our experiments in Section 2. A comparison of those experiments allows for a robust examination, presented in Sections 3 and 4, of tropical rainfall systems across multiple scales—from the ITCZ to equatorial waves to organized precipitation systems. Conclusions and implications of our results are discussed in Section 5.

2. Methods

2.1. Experimental Design

Simulated tropical rainfall systems were examined in a set of aquaplanet simulations using version 6.2 of the Model for Prediction Across Scales-Atmosphere (MPAS-A; Skamarock et al., 2012), which is a nonhydrostatic atmospheric modeling system using an unstructured grid. Rios-Berrios et al. (2020a); Rios-Berrios et al. (2020b) documented the aquaplanet configuration of MPAS-A, showing that MPAS-A captured a stronger signal associated with convectively coupled equatorial waves than many other general circulation models. The simulations presented here use the same configuration as in Rios-Berrios et al. (2020a); Rios-Berrios et al. (2020b) following the design of APE (Blackburn & Hoskins, 2013): a zonally-symmetric, temporally-fixed SST given by the observed (“QOBS”) profile (Neale & Hoskins, 2001), a perpetual equinox, hemispherically symmetric ozone, and radiatively-inactive aerosols.

Four experiments were produced spanning the horizontal grid spacings typically used by climate models, operational numerical weather prediction models, and next-generation models with storm-resolving resolution in the tropics. The first three experiments, which were also analyzed by Rios-Berrios et al. (2020a); Rios-Berrios et al. (2020b), used uniform cell spacing of 120, 30, and 15 km everywhere. The fourth experiment is the first of its kind, employing a variable-resolution mesh with 3 km cell spacing between 20°S and 20°N gradually transitioning to 15 km cell spacing poleward of 30°S and 30°N. Each experiment had a time step and horizontal diffusion length scale proportional to its horizontal grid spacing (Table 1). The vertical grid, which is the same for all experiments, contained 75 vertical levels stretching from 60 m spacing near the surface to 500 m between 10 and the model top at 40 km. A Rayleigh vertical velocity damping was applied above 30 km height.

All experiments used the same physics packages. Cloud microphysics processes were parameterized with the Weather Research and Forecasting Single Moment six Class scheme (Hong et al., 2006), and subgrid-scale turbulence was parameterized with the Yonsei University boundary-layer scheme (Hong et al., 2004). The Rapid Radiative Transfer for GCMs radiation scheme was used for both longwave and shortwave radiation (Iacono et al., 2008) with sub grid-scale cloud fraction calculated from grid-scale relative humidity, water vapor mixing ratio, and cloud and ice mixing ratios following Xu and Randall (1996). The new Tiedtke convection scheme (Zhang & Wang, 2017) was used for deep and shallow convection, except an experimental scale-aware function was added to reduce the effect of deep convection for cell spacings smaller than 15 km (Wang, 2022). Over 90% of the tropical rainfall is explicitly resolved in the 3 km experiment in comparison to only 5% in the other

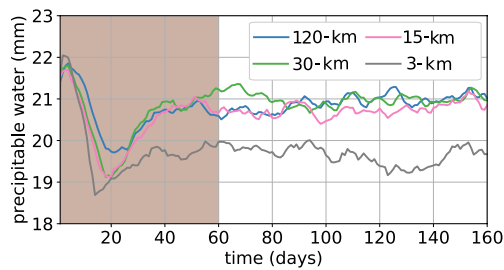


Figure 1. Time series of globally averaged precipitable water from the 120 (blue), 30 (green), 15 (pink), and 3 km (gray) experiments. Light brown shading indicates the spinup period.

experiments; therefore, we will refer to the 120, 30, and 15 km experiments as having parameterized deep convection and to the 3 km experiment as having resolved deep convection.

All experiments reach statistical equilibrium after about 60 days. This is illustrated by Figure 1, showing the globally-averaged precipitable water vapor. Experiments with parameterized convection were integrated for a total of 790 days (i.e., 2 years and 2 months) while the 3 km experiment was integrated for 160 days because of the computational expense. One difference is that the 3 km experiment has a drier atmosphere; specifically, the experiments with parameterized convection equilibrate at a globally-averaged precipitable water of approximately 21 mm, and the 3 km experiment equilibrates at a globally-averaged value just below 20 mm. This difference may be associated with more removal of water vapor by more intense precipitation in the tropics in the storm-resolving experiment, as will be shown below. For purposes of comparison, the first 60 days were considered model spinup and were not used in the forthcoming analysis.

Despite its shorter integration time and variable resolution mesh, the 3 km experiment develops the expected mean climate from an aquaplanet configuration with zonally-symmetric SST (Figure 2). The warmest air and highest tropopause appear in the tropics, where zonally-averaged easterlies also exist throughout the troposphere (Figure 2a). Moist ascending air, associated with a Hadley circulation, also appears in the tropics and is flanked by dry descending air in the subtropics (Figure 2b). The Hadley circulation extends until approximately 25.5° latitude as estimated from the mass streamfunction described by Rios-Berrios et al. (2020a). Westerly jets appear in the middle latitudes along with relatively strong temperature gradients. The maximum zonally averaged, time-averaged zonal wind is approximately 48 m s⁻¹ at 32° latitude. Overall, the general circulation is very similar to that produced by the parameterized convection experiments (cf. Figure 2 with Figure 3 from Rios-Berrios et al., 2020a; 2020b). These results demonstrate that the experiment with variable resolution produces a mean

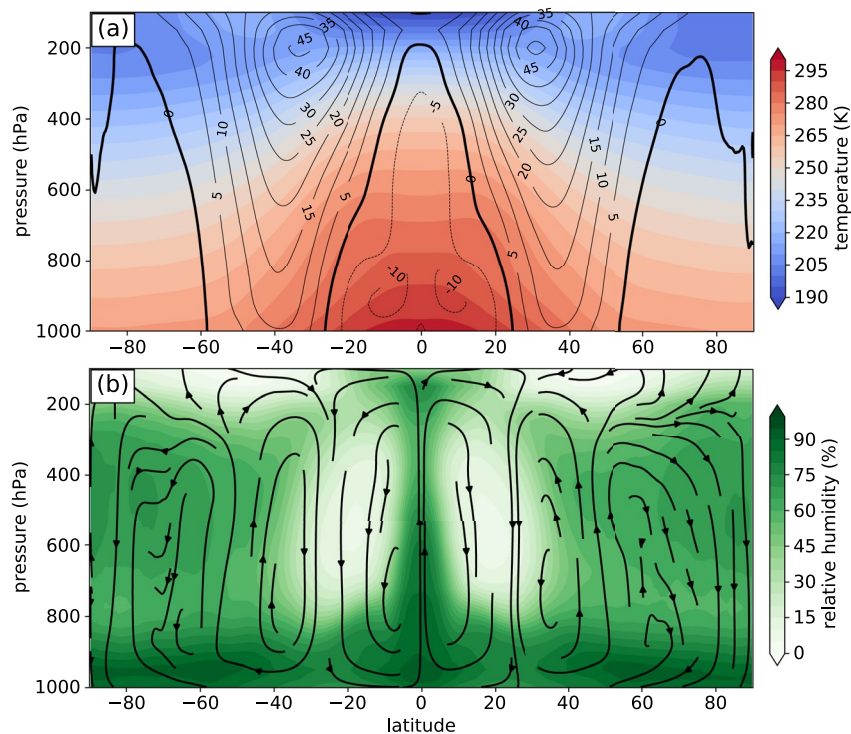


Figure 2. Time-averaged, zonally-averaged (a) temperature (shading, every 5 K) and zonal wind (contours, every 5 m s⁻¹), and (b) relative humidity (shading, every 5%) and meridional circulation (streamlines) from the 3 km MPAS-A simulation. In panel (a), solid contours represent westerlies and dashed contours represent easterlies.

climate that, with the exception of being slightly drier, is consistent with the mean climate from the uniform resolution experiments.

2.2. Diagnostics

Model output from each simulation was conservatively regridded from the unstructured MPAS-A mesh to a Gaussian grid using the Climate Data Operator tool. For time-averaged, zonally averaged analyses, the interpolated output was on an n80 Gaussian grid with approximately 1.25° latitude-longitude spacing in the tropics. For everything else (i.e., Sections 3.2–4), the output was interpolated to an n256 Gaussian grid. The equivalent grid spacing in the tropics of the n256 grid is approximately 0.351° latitude-longitude grid spacing, which captures most of the details of the 30, 15, and 3 km experiments. Whenever possible, the interpolated output from each hemisphere was averaged as a function of latitude to effectively double the sample size. This hemispheric averaging masks out subtle hemispheric asymmetries that exist in the middle and polar latitudes of the 3 km experiment, which are not the focus of this study.

2.2.1. Objective ITCZ Identification

An objective ITCZ identification algorithm was used with the n80 interpolated output to compare ITCZ characteristics amongst the aquaplanet experiments. The algorithm closely follows the steps of Berry and Reeder (2014). ITCZ segments were defined as continuous grid points satisfying the following criteria on 14 days running mean output (Figure S1 in Supporting Information S1):

1. Convergent boundary-layer winds given by the 925–1,000 hPa layer-averaged convergence
2. A positive Laplacian of the meridional divergence of boundary-layer winds (indicative of a maximum in convergence)
3. 850 hPa wet bulb temperature exceeding 300 K, and
4. The above conditions must exist for a continuous 35° or larger longitudinal segments

With these criteria, the ITCZ position was identified on daily output from each experiment, thus providing a large sample to analyze the ITCZ latitudinal location on each hemisphere (in the case of double ITCZs) or along the equator (in the case of a single ITCZ). This objective ITCZ identification method yields a more robust analysis than time-mean zonal-mean rainfall diagnostics. Additionally ITCZ width was determined by the latitudinal extent of the 5 mm day^{-1} contour away from the ITCZ points, and ITCZ intensity was defined by the rainfall rate at the ITCZ grid points.

2.2.2. Convectively Coupled Equatorial Waves

Convectively coupled equatorial waves were identified, tracked, and analyzed from the n256 interpolated output for a 100 day period. That period was the entire analysis period of the 3 km experiment and the last 100 days of the other experiments. We focused on the dominant equatorial waves in aquaplanet simulations as described by Nakajima et al. (2013): Kelvin waves, advective disturbances, and $n = 1$ inertio-gravity waves. Here, Kelvin waves are defined as eastward-propagating disturbances with a time period of 2.5–20 days and wavenumbers 1–14, advective disturbances are westward-propagating disturbances with a time period of 2.5–20 days and wavenumbers 4–28 (these are similar to easterly waves in the real atmosphere), and $n = 1$ inertio-gravity waves are westward-propagating disturbances with a time period of 1.8–4.5 days and wavenumbers 1–14. These waves were identified using a similar method of Wheeler and Weickmann (2001) with the following steps:

1. Meridionally averaging the 6-hourly rainfall rates between 10°S and 10°N
2. Zero-padding the meridionally averaged rainfall rate by adding 700 time steps with all zeroes (to prevent spectral leaking; Wheeler & Weickmann, 2001)
3. Applying a fast Fourier transform in both space and time
4. Zeroing out all frequencies and wavelengths outside the desired thresholds for each wave, and
5. Applying an inverse fast Fourier transform on the retained data

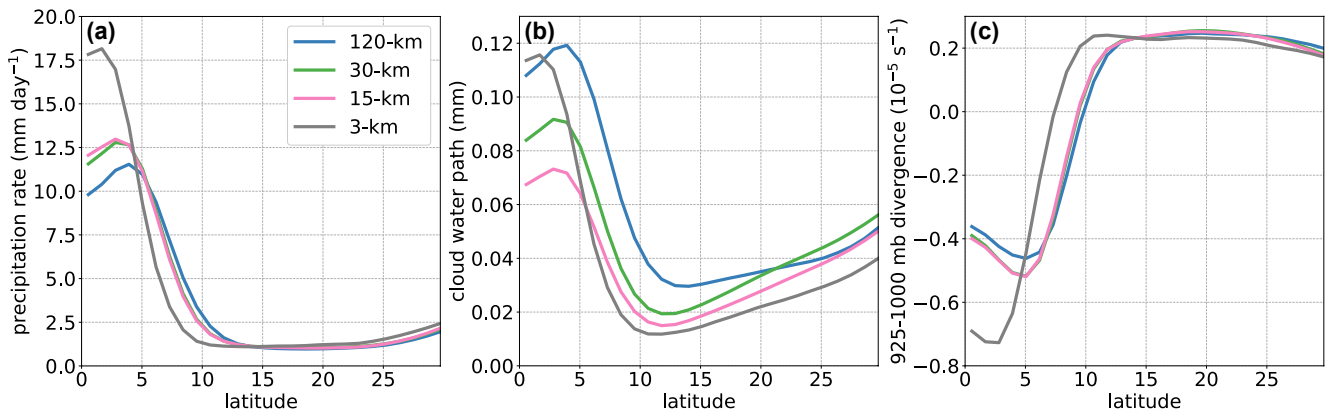


Figure 3. Zonally averaged, time-averaged (a) precipitation rate (b) grid-scale cloud water path, and (c) 925–1,000 mb divergence. Four experiments are shown: 120 (blue), 30 (green), 15 (pink), and 3 km (gray).

This method yields filtered rainfall rate anomalies for each wave. Those anomalies were then used to identify the location of each wave peak, which is given by grid points where the first temporal derivative of the filtered anomalies is zero and the corresponding second derivative is negative (Figure S2 in Supporting Information S1). Those anomalies and peak locations were used to compare the equatorial waves across experiments.

2.2.3. Organized Precipitation Systems and Cold Pools

Organized precipitation systems were defined as continuous rainy grid points as identified using an object-tracking approach with the Method for Object-based Diagnostic Evaluation (MODE; Davis et al., 2009). While MODE was originally designed to compare model output against observations, MODE can also be used to identify any kind of objects (i.e., regions of interest) from model output (e.g., Prein et al., 2017). Object identification in MODE follows a “convolution thresholding” approach with three basic steps:

1. Convoluting (i.e., smoothing) the field of interest in space,
2. Applying a mask to retain values only above or below a desired threshold, and
3. Identifying individual objects as the connected grid points inside the mask

After the initial identification of objects, MODE combines objects that are close enough to each other to be considered part of the same system. MODE additionally calculates several diagnostics for each final object, including its location, intensity, area, angle of orientation, etc. Here, we used MODE with rainfall rates to identify organized rainfall systems and with 2-m virtual temperature anomaly (from a zonal mean) to identify cold pools. Both fields were convolved with a radius of two n256 grid points. More details on thresholds and output will be provided in Section 4, and an example of rainfall systems identified by MODE is shown in Figure S3 of Supporting Information S1.

3. Effects of Resolved Deep Convection

3.1. ITCZ and Subtropics

Storm-resolving resolution has a large impact on the ITCZ structure as demonstrated by zonally averaged, time-averaged metrics (Figure 3). In these metrics, the 3 km experiment shows peak rainfall rates of 19 mm day⁻¹ at approximately 2° latitude with a steep decrease toward a subtropics minimum of 1 mm day⁻¹ at 10° latitude (Figure 3a). The cloud water path exhibits a consistent structure with peak cloudiness at 2° latitude and a rapid decrease toward the subtropics minimum at 10° latitude (Figure 3b). In contrast, all experiments with parameterized deep convection exhibit weaker peak rainfall rates of approximately 11 mm day⁻¹ in the 120 km experiment and approximately 13 mm day⁻¹ in both the 30 and 15 km experiments. Those peaks are also 3–4° poleward of the peak in the 3 km experiment, and are associated with a slower decrease toward a minimum of 1 mm day⁻¹

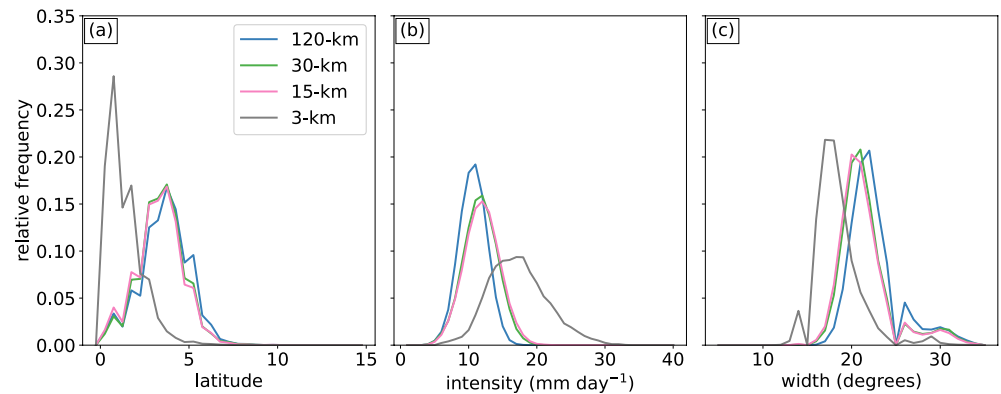


Figure 4. Probability density functions of objectively identified (a) intertropical convergence zone location, (b) intensity, and (c) width for the 120 km (blue), 30 km (green), 15 km (pink), and 3 km (gray) experiments.

poleward of 13° latitude. Kinematic metrics, such as boundary-layer convergence (Figure 3c), further support this key difference between experiments. The 3 km experiment is associated with peak convergence of $0.75 \times 10^{-5} \text{ s}^{-1}$ between 1° and 2° latitude, which is about 50% stronger and 2° and 3° equatorward of the peak convergence of $0.5 \times 10^{-5} \text{ s}^{-1}$ at 5° latitude in all other experiments.

The parameterized convection experiments also show differing cloudiness, as shown by the zonally-averaged, time-averaged cloud water path (Figure 3b). Their amount of cloud water in the tropics decreases with decreasing cell spacing amongst those experiments, but their peaks are consistently located with their rainfall peaks. Such variability can affect the top-of-atmosphere radiation budgets through variability in cloud-radiative feedbacks (not shown).

Objective metrics of ITCZ location, intensity, and width confirm that resolved deep convection yields a more equatorward, stronger, and narrower ITCZ than parameterized deep convection (Figure 4). The probability density function (PDF) of ITCZ location from the 3 km experiment exhibits a stronger peak and narrower distribution than in all other experiments (Figure 4a). This result demonstrates that the 3 km experiment consistently has convergent motions close to or at the equator—even on daily time scales. Meanwhile, the experiments with parameterized convection are associated with a more poleward and more variable ITCZ location as demonstrated by their wider PDFs with peak frequency at 4° latitude. Substantial differences also exist in the PDF of ITCZ intensity (Figure 4b): while the 3 km experiment is associated with a wide distribution of rainfall rates between 5 and 30 mm day^{-1} , the experiments with parameterized deep convection are associated with narrow distributions peaking at 12 mm day^{-1} . Lastly, the PDF of ITCZ width confirms that the ITCZ of the 3 km is narrower than the ITCZ of the other experiments (Figure 4c). The PDF of the 3 km experiment is shifted toward smaller values and is associated with a peak at 18° , which is at least 5° narrower than the peak of the experiments with parameterized deep convection.

Motivated by previous work on ITCZ dynamics (Gonzalez & Schubert, 2019; Möbis & Stevens, 2012; Williamson et al., 2013), we compared zonally averaged, time-averaged boundary-layer and midtropospheric metrics from our MPAS-A aquaplanet experiments (Figure 5). These metrics show that the 3 km experiment has a steeper meridional gradient of both boundary-layer moist static energy and midtropospheric relative humidity poleward of 5° and 2.5° latitude, respectively (Figures 5a and 5b). In contrast, all other experiments have a broad peak in the tropics and a relatively weaker meridional gradient of boundary-layer moist static energy and midtropospheric relative humidity poleward of 7.5° and 5° latitude, respectively. These results are consistent with the view that an equatorward ITCZ position is associated with steeper meridional thermodynamic gradients, which support convection close to the equator (Möbis & Stevens, 2012). However, the magnitude of these thermodynamic metrics alone cannot explain the different ITCZ intensity because the 3 km experiment has comparable peak boundary-layer moist static energy (339 J kg^{-1}) and midtropospheric humidity (81%) to all other experiments.

Instead, the ITCZ behavior in these experiments is likely responding to and affecting multiple processes, including dynamics in the boundary layer. Even though the peak magnitude of zonally averaged, time-averaged zonal

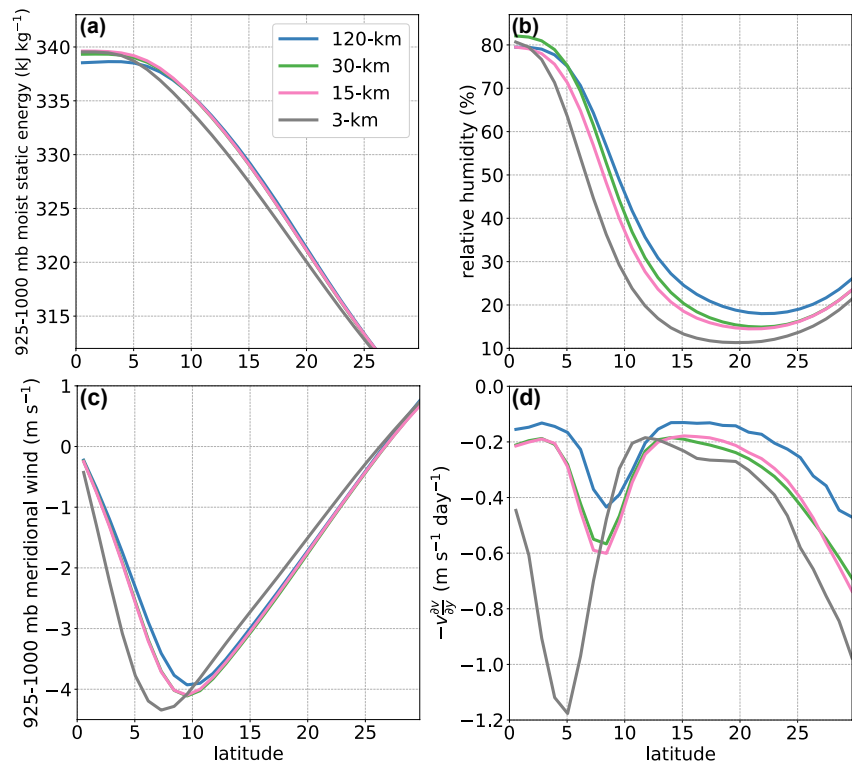


Figure 5. Zonally averaged, time-averaged (a) 925–1,000 mb moist static energy, (b) 500–700 hPa relative humidity, (c) 925–1,000 mb meridional wind, and (d) 925–1,000 mb meridional momentum advection by the meridional wind.

and meridional winds are comparable amongst all experiments, the 3 km experiment stands out from the rest in the location of that peak and in the strength of the meridional gradient of the meridional wind (Figure 5c). Specifically, this experiment is associated with a peak boundary-layer meridional wind of 4.5 m s^{-1} at 7° latitude and a rapid decrease in magnitude toward the equator. In contrast, the other experiments have peak boundary-layer meridional winds of 4 m s^{-1} at 10° latitude (Figure 5c). These differences are important because nonlinear meridional momentum advection can modulate the intensity and location of the ITCZ as shown by Gonzalez and Schubert (2019). Consistent with that study, the narrower and stronger ITCZ in the 3 km experiment is associated with twice as strong meridional advection of meridional wind that peaks about $3\text{--}4^\circ$ closer to the equator than in all other experiments (Figure 5d).

A noteworthy result from this analysis is the close similarity between the experiments with parameterized convection. The 30 and 15 km exhibit nearly identical rainfall rates, boundary-layer winds, boundary-layer moist static energy, and lower tropospheric ascent (not shown) in the tropics. Those metrics are weaker in the 120 than in the 30 and 15 km experiments, but the general pattern is similar between all three experiments. Such similarity demonstrates that increasing the horizontal model resolution—while parameterizing deep convection—results in little change to the time-mean structure of the tropics in MPAS-A aquaplanet experiments.

3.2. Tropical Rainfall Variability

Our MPAS-A aquaplanet experiments also expose the effects of resolved deep convection on tropical rainfall variability. Those effects are examined qualitatively with Hovmöller diagrams of raw and filtered precipitation rates from the n256 interpolated output averaged between 10°S and 10°N (Figures 6 and 7). Rainfall variability is evident in the raw rainfall by periods of relatively heavy precipitation followed by periods of light or no precipitation (Figure 6). There is a strong similarity between all experiments: tropical rainfall variability is primarily driven by eastward propagating features. Those features correspond to Kelvin waves as demonstrated by the filtered rainfall (Figure 7). An important difference is that the 3 km experiment shows more periods of

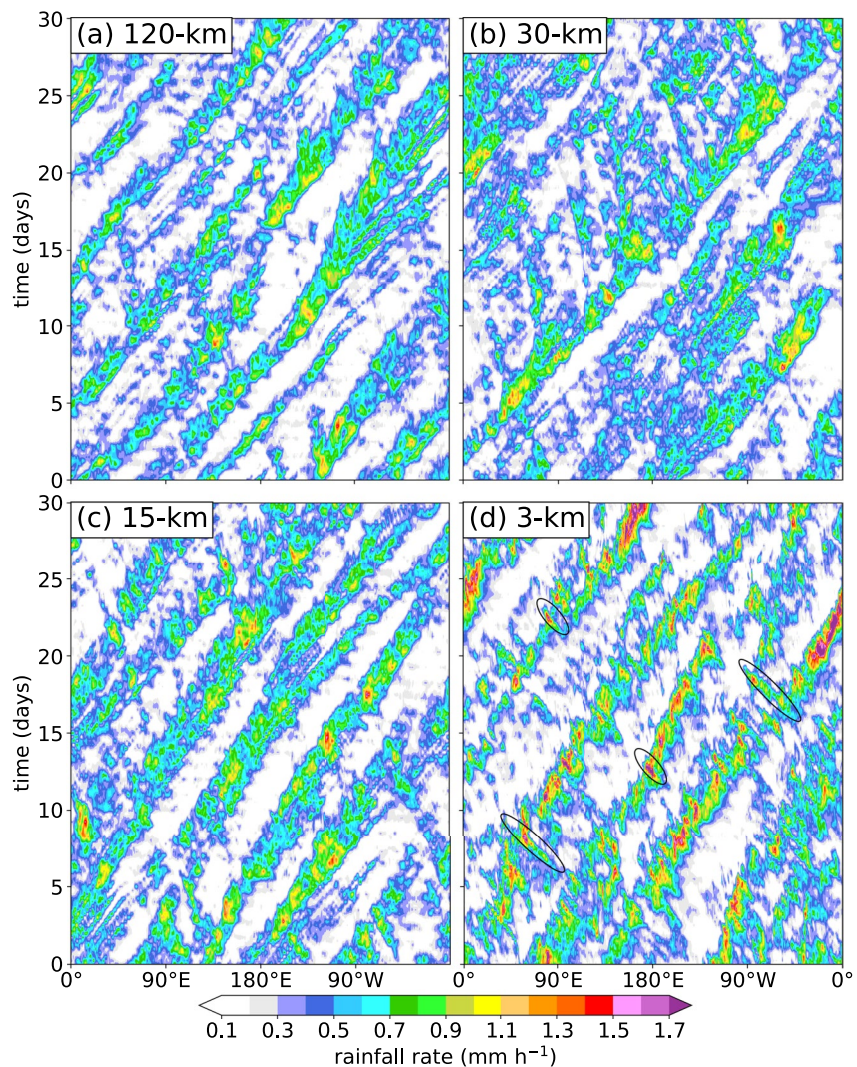


Figure 6. Hovmöller diagrams of 6-hourly precipitation rate (shading, every 0.1 mm hr^{-1}) averaged between 10°S and 10°N from MPAS-A simulations using (a) 120, (b) 30, (c) 15, and (d) 3 km cell spacing. Ovals in panel (d) show examples of westward propagating features.

high-intensity precipitation driven by short-lived and often westward propagating features that are much weaker in the other experiments (see ovals in Figure 6d). These short-lived features project primarily into $n = 1$ westward inertio-gravity waves; while they are present in all simulations, these waves happen *more frequently* and can be up to three times stronger in the 3 km experiment than in the other experiments (0.3 mm hr^{-1} vs. 0.1 mm hr^{-1} ; Figure 7).

A quantitative analysis further illustrates the differences between simulations. Figure 8a shows the variance of rainfall rates averaged between 10°S and 10°N over a 100-day period. Consistent with the qualitative analysis, the experiments with parameterized deep convection exhibit comparable rainfall variance of approximately $0.05 \text{ mm}^2 \text{ hr}^{-2}$. This indicates that rainfall variability is similar amongst those experiments despite their horizontal resolutions spanning an order of magnitude. On the other hand, there is a much more pronounced increase in rainfall variability from 15 to 3 km cell spacing: the total variance from the 3 km experiment is double the total variance from the 120 and 30 km experiments. This result indicates that resolved deep convection results in more day-to-day variability of synoptic-scale tropical systems, which is consistent with the real-data forecasts analyzed by Judt and Rios-Berrios (2021).

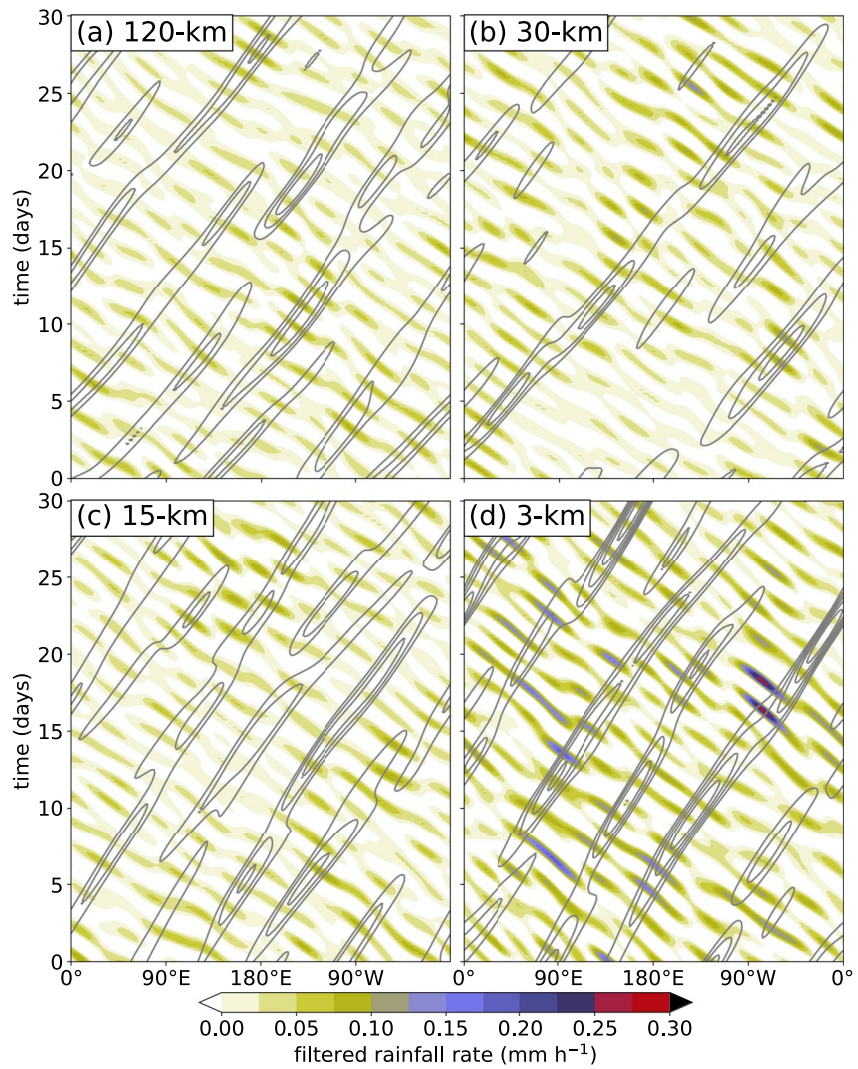


Figure 7. Hovmöller diagrams of filtered 6-hourly precipitation rate associated with westward inertio-gravity waves (shading, every 0.025 mm hr^{-1}) and Kelvin waves (contours, every 0.125 mm hr^{-1}) from MPAS-A simulations using (a) 120, (b) 30, (c) 15, and (d) 3 km cell spacing.

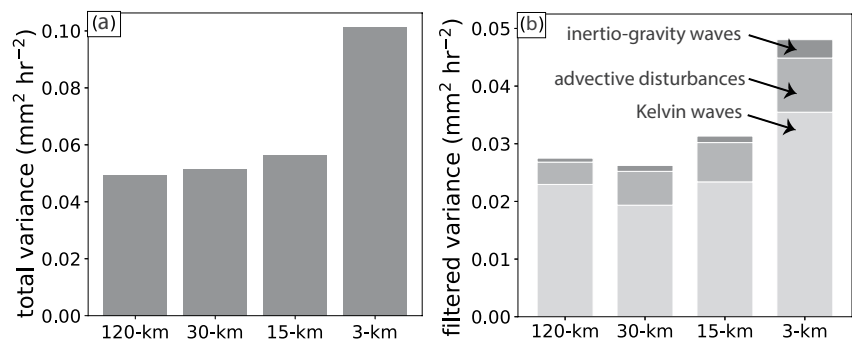


Figure 8. (a) Total and (b) wave-filtered precipitation rate variance per each experiment. In panel (b), light gray represents Kelvin waves, medium gray represents advective disturbances, and dark gray represents westward inertio-gravity waves.

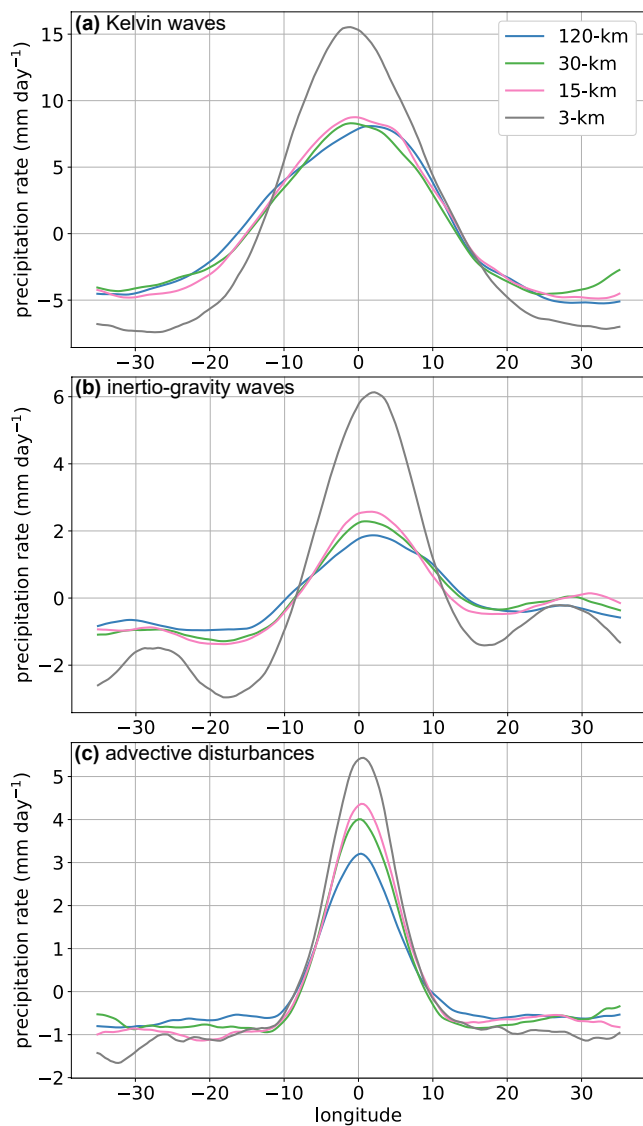


Figure 9. Wave-relative composites of rainfall rate anomalies associated with (a) Kelvin waves, (b) $n = 1$ inertio-gravity waves, and (c) advective disturbances from MPAS-A simulations using 120 (blue), 30 (green), 15 (pink), and 3 km (grey) cell spacing.

whereas that peak is approximately 4 mm hr^{-1} in both the 30 and 15 km experiments and 3 mm hr^{-1} in the 120 km experiment. Away from the peak, all experiments—including the 3 km experiment—show decreasing composite rainfall anomalies reaching a minimum between -0.5 and -1.0 mm hr^{-1} . Compared to Kelvin and inertio-gravity waves, the effects of resolved deep convection are less pronounced on advective disturbances. A forthcoming study will examine this result in more detail.

Rainfall variability was further compared between experiments by comparing rainfall variance associated with convectively coupled equatorial waves. Figure 8b shows that comparison; this figure is similar to Figure 8a, except for showing the variance of rainfall rate anomalies associated with Kelvin waves, advective disturbances, and inertio-gravity waves. This partition of wave-filtered precipitation variance exposes both similarities and differences between the disturbances that are captured by our MPAS-A aquaplanet simulations. All experiments exhibit the largest variance for Kelvin waves, followed by advective disturbances and inertio-gravity waves. The dominant role of Kelvin waves in these aquaplanet experiments is consistent with the qualitative analysis that showed eastward-propagating rainfall associated with Kelvin waves regardless of horizontal resolution (Figures 6 and 7).

Advective disturbances and inertio-gravity waves exhibit the largest difference in this quantitative comparison of rainfall variability. The variance associated with westward advective disturbances increases with increasing horizontal resolution, such that the variance of the 3 km experiment is at least 75% larger than in any of the experiments with parameterized deep convection. Westward-propagating inertio-gravity waves exhibit the most pronounced differences between experiments. Specifically, these waves are more active with resolved deep convection than with parameterized deep convection—their filtered variance in the 3 km experiment is at least 200% larger than in any of the other experiments. This much larger variance reflects both their more frequent and stronger signals in the 3 km experiment (Figure 7).

Our experiments also demonstrate that the rainfall structure of convectively coupled equatorial waves is substantially different with resolved deep convection. This result is shown in Figure 9 through wave-relative composites of rainfall rate anomalies. The wave peak was identified as described in Section 2c. The equatorial waves in the 3 km experiment are associated with stronger rainfall rates at their peaks. This result is true for all waves, but it is most evident for Kelvin waves (Figure 9a) and inertio-gravity waves (Figure 9b) for which the maximum rainfall anomalies from the 3 km experiment is almost three times larger than the maximum from each of the experiments with parameterized convection. Weber et al. (2020) obtained a similar result in their analysis of a single Kelvin wave: the wave peak was much stronger (and more similar to observations) with resolved deep convection.

Away from the peak, the effects of storm-resolving resolution on rainfall structure depend on the wave type. Kelvin waves and inertio-gravity waves are associated with sharper rainfall rate gradients toward and away from their stronger peaks in the 3 km experiment (Figures 9a and 9b). This result implies that these waves are not only stronger but also zonally narrower when deep convection is resolved. In contrast, advective disturbances primarily differ in the magnitude of their rainfall peaks (Figure 9c); the composite peak of rainfall rate anomalies from the 3 km experiment is approximately 5 mm hr^{-1} ,

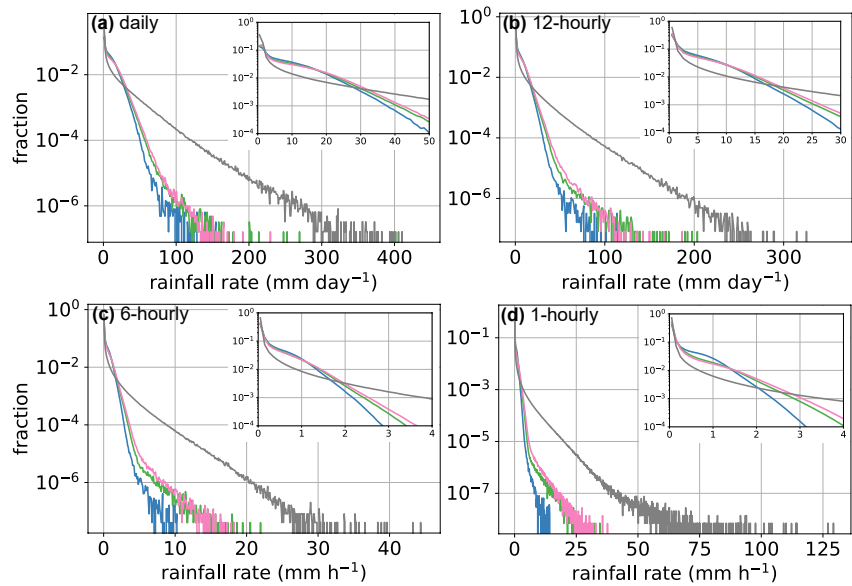


Figure 10. Distributions of rainfall rates from the 120 (blue), 30 (green), 15 (pink), and 3 km (grey) experiments. Each panel shows a different time period: (a) daily rainfall rates, (b) 12 hourly rainfall rates, (c) 6 hourly rainfall rates, and (d) 1 hourly rainfall rates. Inset shows zoomed in distributions for the lowest rainfall rate bins. Note the different units for the top and bottom panels.

3.3. Rainfall Extremes

A common theme so far is that resolved deep convection in the tropics yields more intense rainfall rates at the planetary and synoptic scales. We further examine if that result could be generalized by comparing distributions of rainfall rates from all grid points between 10°S and 10°N in the n256 interpolated output (Figure 10). Given that the native output was conservatively regrided, a comparison of the interpolated output facilitates comparison across all experiments. We also considered different time scales by examining the distributions for daily (Figure 10a), 12 hourly (Figure 10b), 6 hourly (Figure 10c), and hourly (Figure 10d) rainfall rates. This analysis only considered the last 100 days from each simulation.

Resolved deep convection results in stronger rainfall rates across all timescales in our MPAS-A experiments. Whether we consider daily or sub-daily rainfall rates, the fraction of heavy rainfall rates ($\geq 48 \text{ mm day}^{-1}$ or 2 mm hr^{-1} ; Trenberth & Zhang, 2018) is at least two orders of magnitude larger in the 3 km experiment than in the experiments with parameterized deep convection (Figures 10a and 10b). This result stems from a smaller fraction of light rainfall rates when deep convection is explicitly resolved. The experiments with parameterized convection produce too much light rain too often, which is consistent with real-data forecasts from other global models (Becker et al., 2021; Jutd & Rios-Berrios, 2021; Stephens et al., 2010). Additionally, the distributions of daily and 12 hourly rainfall rates from the 3 km experiment intersect all other experiments around 30 and 17 mm day^{-1} , respectively. Beyond those values, the distribution from the 3 km experiment exhibits a long tail with daily rainfall rates reaching up to 400 mm day^{-1} and 12 hourly rainfall rates of up to 310 mm day^{-1} . In contrast, the extreme rainfall rates from the other experiments are under 300 mm day^{-1} regardless of horizontal resolution.

Similarly, the distributions of 6 hourly and hourly rainfall rates from the 3 km experiment intersect all other distributions around 1.9 and 5 hr^{-1} , respectively (Figures 10c and 10d). The larger values beyond that intersection imply that the 3 km experiment is associated with stronger rainfall extremes than other experiments, which could explain the more intense rainfall rates from the ITCZ to individual equatorial waves. However, it is unclear if the more intense rainfall extremes of the 3 km experiment are too intense or if those extremes would be even stronger without the scale-aware cumulus parameterization. More analysis with real-data forecasts compared against observations are needed to clarify this point.

Rainfall rates over the tropical ocean increase exponentially beyond critical values of saturation fraction (SF) (Ahmed & Schumacher, 2017; Bretherton et al., 2004; Neelin et al., 2009) and lower-tropospheric plume

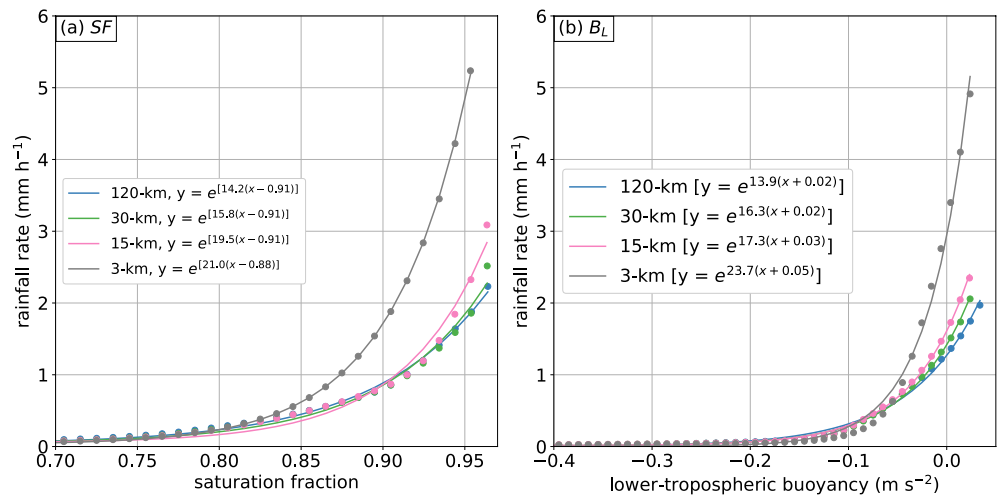


Figure 11. Conditionally averaged rainfall rate as a function of (a) saturation fraction (SF) separated into 0.01 bins and (b) lower-tropospheric plume buoyancy (B_L) separated into 0.01 m s^{-2} bins. The legend shows the exponential fit for the (blue) 120, (green) 30, (pink) 15, and (gray) 3 km experiments.

buoyancy (B_L) (Ahmed et al., 2020). SF, also known as column relative humidity, is the ratio of precipitable water vapor to saturated precipitable water vapor. B_L measures the buoyancy of parcels exiting the boundary layer and is defined as

$$B_L = \frac{g}{e_L^*} \Pi_L \left(\frac{w_B e_B}{\Pi_B} + \frac{w_L e_L - e_L^*}{\Pi_L} \right),$$

where e is moist enthalpy $\left[e = T + \left(\frac{L_v}{c_p} \right) q_v \right]$, Π is the Exner function, g is gravity, subscript L represents lower-tropospheric layer (500–850 hPa), subscript B represents the boundary layer (850–1,000 hPa), and w_L and w_B are weighting functions set as 0.52 and 0.48 (Ahmed et al., 2020).

Conditionally averaging 6 hourly rainfall rates as a function of binned SF (Figure 11a) or binned B_L (Figure 11b) shows different moisture-rainfall relationships between the experiment with resolved deep convection and the other experiments. Rainfall rates exhibit a slightly earlier and steeper exponential increase when deep convection is resolved than when it is parameterized. An exponential fit to the conditionally-averaged rainfall rates indicate that the exponential increase begins when SF is 0.88 in the 3 km experiment but when SF is 0.91 in the other experiments. Likewise, an exponential fit with B_L indicates that rainfall rates begin their exponential increase when B_L is -0.05 in the 3 km experiment but -0.02 in the 30 and 15 km experiments. This indicates that the highest rainfall rates happen at moderately moist environments when deep convection is resolved. At the same time, the smaller rainfall rates for the same SF or B_L in the experiments with parameterized convection suggests that those experiments cannot resolve weather phenomena that produce moderate-to-heavy rainfall beyond the critical values of moisture and buoyancy.

The above results underscore the impacts of resolved deep convection because this comparison was done on the same grid scale despite the different cell spacing during model integration. The similarities between experiments with parameterized deep convection—together with the substantially different distributions from the 3 km experiment—further emphasize that the different fractions of heavy and extreme rainfall rates stem primarily from the resolved convection and not from the different cell spacings between experiments. It is possible that these results depend on the convection scheme, such that the Tiedtke scheme is deficient at accounting for small-scale precipitation systems that produce extreme precipitation and that are explicitly captured with resolved deep convection.

Table 2
Summary of the Amount of Precipitation Systems and Cold Pools Identified With MODE

Simulation name	Precipitation systems	Cold pools
30 km	15,941	390
15 km	15,640	1,160
3 km	15,024	6,368

4. Organized Precipitation Systems

The larger fraction of heavy rainfall—from hourly to daily timescales—demonstrates that resolved deep convection captures robust rain-producing phenomena that are either weaker or different at coarse resolution with parameterized deep convection. We suspect that this result stems from differences in the common unit of all tropical rain-producing phenomena: organized precipitation systems. Tropical clouds and precipitation frequently happen in clusters or regions of organized convection ranging from meso to planetary scales. Organized precipitation systems are known as the “building blocks” of tropical convection—their evolution from shallow to deep convection

to stratiform precipitation is characteristic of rainfall production in the tropics across different spatiotemporal scales (Mapes et al., 2006). Therefore, it is likely that resolved deep convection can affect the characteristics of organized precipitation systems in our aquaplanet experiments, which in turn can feedback onto planetary-scale and synoptic-scale systems.

We investigated this possibility through a comparison of organized precipitation systems from our MPAS-A aquaplanet experiments. Here, an organized precipitation system is defined as a group of three or more contiguous grid points (from the n256 interpolated output) with rainfall rates of 0.9 mm hr^{-1} or larger. The number of grid points ensures that the system covers at least $10,000 \text{ km}^2$, which is well inside the area of observed mesoscale convective systems (see Figure 40 of Houze 2004). Moreover, the rainfall rate threshold was chosen because the cumulative density functions of 6-hourly rainfall rates from the 3 km experiment intersect all other experiments at 0.9 mm hr^{-1} (not shown). Our results are insensitive to the area and rainfall thresholds. Organized precipitation systems were identified with MODE as described in Section 2c. We identified over 15,000 systems over a 100 day period in each experiment (Table 2) which allows for a robust statistical analysis (we only present results from the 30, 15, and 3 km experiments because the 120 km experiment was very similar to the 30 and 15 km experiments). The latitudinal distribution of centroid location from each system (Figure 12a) is consistent with the aforementioned results: the 3 km experiment captures more precipitation systems at lower latitudes than the rest of experiments. This comparison of organized precipitation systems can, therefore, inform how mesoscale and synoptic-scale phenomena are linked to the different ITCZ and equatorial waves characteristics across experiments.

Resolved deep convection yields organized precipitation systems with higher volumetric rainfall than parameterized deep convection. This result is shown in Figure 13a through distributions of rainfall volume as diagnosed by MODE. While the mean volume is comparable across experiments, the 75th percentile and the maximum volume

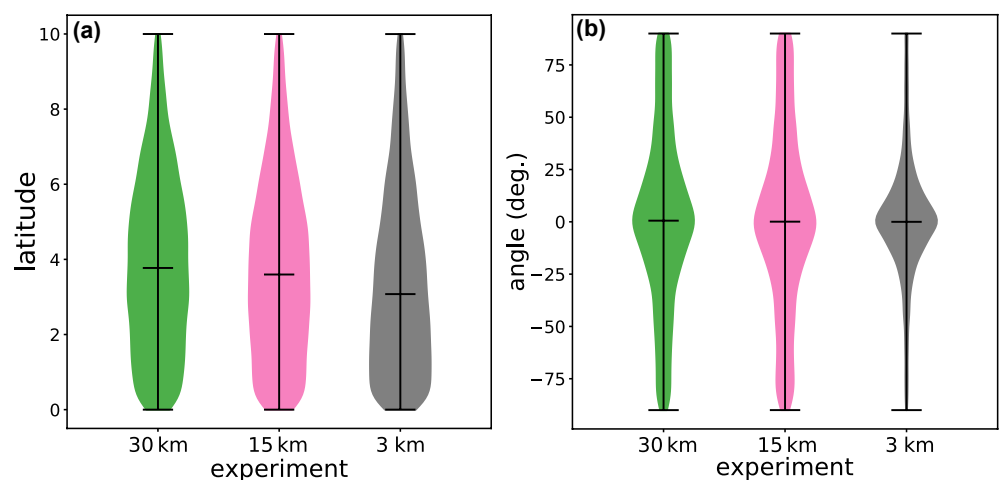


Figure 12. Violin plots showing the distribution of (a) absolute latitude and (b) angle with respect to the horizontal of all rainfall systems in the 30 (green), 15 (pink), and 3 km (gray) experiments. The horizontal line marks the median from each experiment.

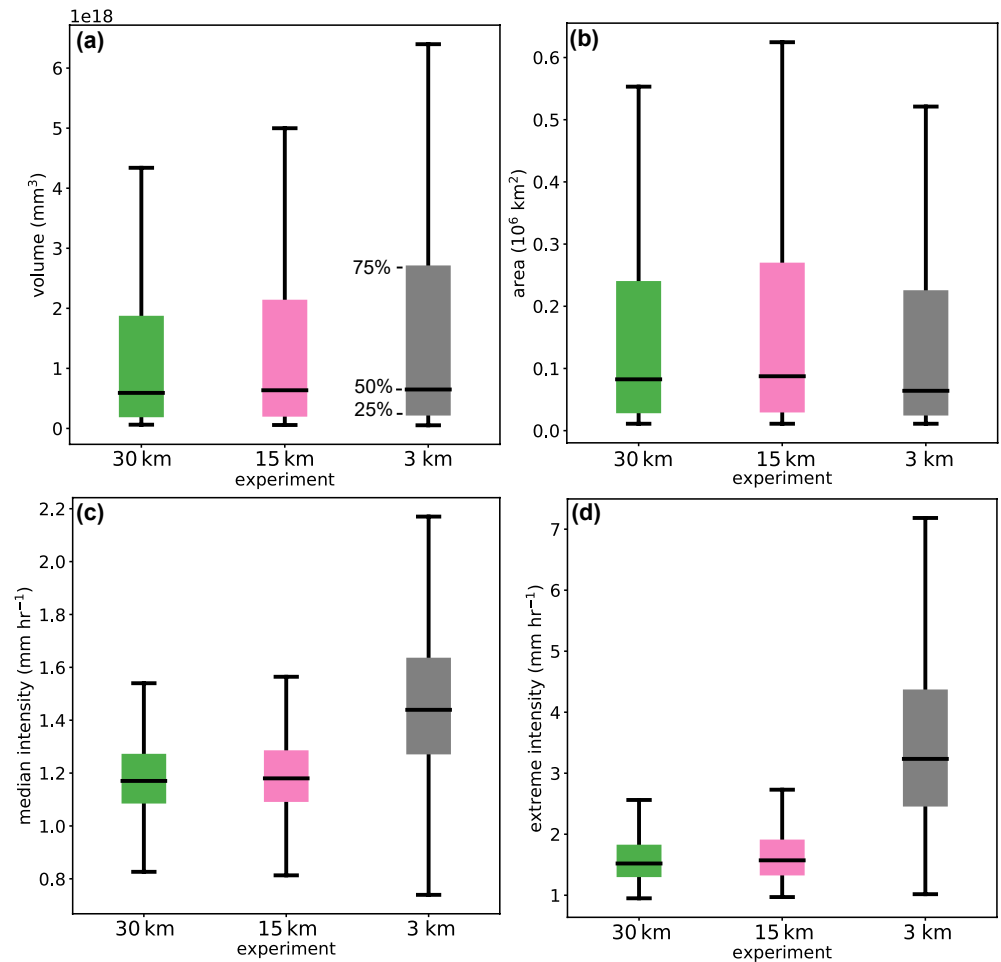


Figure 13. Box plots showing the distributions of (a) total volumetric rainfall, (b) area, (c) median intensity, and (d) extreme intensity from organized precipitation systems in the 30 (green), 15 (pink), and 3 km (gray) experiments. Boxes extend from the 25th to the 75th percentiles, whiskers extend from minima to maxima, and the horizontal line on the box marks the median (or 50th percentile) of each experiment.

from the 3 km experiment are at least 50% larger than from the 30 and 15 km experiments. This means that the 3 km experiment has a wider distribution associated with more heavy rain-producing systems. Evidently, both the 75th percentile and maximum volume increase with increasing horizontal resolution. Volumetric rainfall is a function of both the area of raining points and the rainfall intensity. The distributions of area covered by the 0.9 mm hr⁻¹ contour of each system does not exhibit a clear relationship between horizontal cell spacing and system size (Figure 13b); in fact, the distributions largely overlap with one another and the median areas of the 30 and 3 km experiments are smaller than the median area of the 15 km experiment.

Instead, the larger volumetric rainfall from the 3-km results from more intense rainfall rates as shown by the distributions of median and extreme (i.e., top tenth percentile) rainfall intensity (Figure 13c). The experiments with parameterized deep convection produce nearly identical distributions of rainfall intensities associated with the precipitation systems. The interquartile range of median intensity spans 1.09–1.27 and 1.09–1.28 mm hr⁻¹ for the 30 and 15 km experiments, respectively. Despite their different horizontal cell spacings, the convection parameterization seems to dominate and produce precipitation systems with similar rainfall intensities. In contrast, there is practically a step function going from the 15 to the 3 km experiment; the 25th percentile of extreme precipitation from the precipitation systems in the 3 km experiment is larger than the 75th percentile of all other experiments. Another noteworthy difference is the larger spread of the interquartile range from the 3 km experiment (2.5–4.4 mm hr⁻¹), which indicates that the 3 km experiment captures not only systems with more extreme rainfalls but also a wider spectrum of heavy-rainfall-producing organized systems.

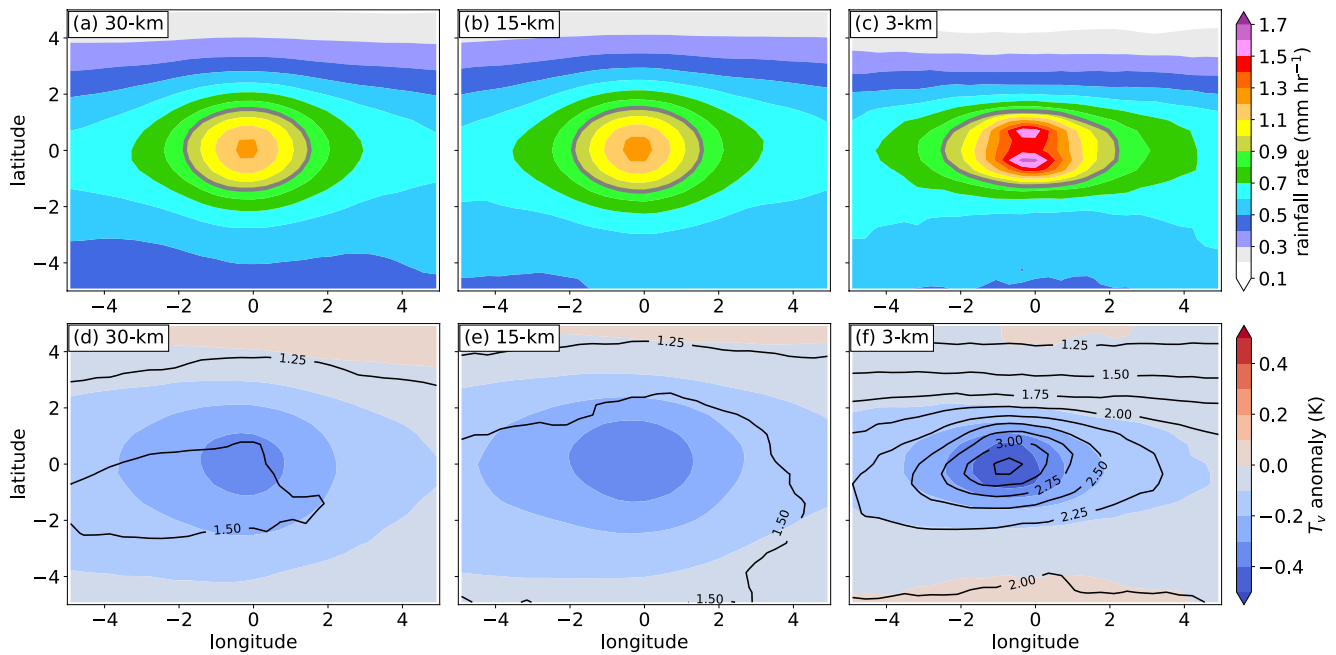


Figure 14. Composite fields relative to the centroid of each rainfall system. Panels show (a–c) rainfall rate (shading, every 0.1 mm hr^{-1} & solid contour showing 0.9 mm^{-1}) and (d–f) 2 m virtual temperature anomaly from the zonal mean (shading, every 0.1 K) and magnitude of the gradient of horizontal wind (contours, every $0.25 \times 10^5 \text{ s}^{-1}$) from the (left) 30, (middle) 15, and (right) 3 km experiments.

To further explore the differences seen in the statistics of rainfall systems, we obtained system-relative¹ latitudes correspond to equatorward (poleward) distance from the system centroid) composites of rainfall rates centered on the centroid latitude and longitude from each system (Figures 14a–14c). The composites of the precipitation systems also demonstrate that, consistent with the previous section, organized precipitation systems produce heavier rainfall rates when deep convection is resolved. The maximum composite rainfall rate is 1.6 mm hr^{-1} in the 3 km experiment and 1.2 mm hr^{-1} in both the 30 and 15 km experiments (Figures 14a–14c). The most intense composite rainfall rates appear near the center of the systems in the experiments with parameterized convection, but away from the centroid in the experiment with resolved deep convection. Double rainfall maxima appear in the composite from the 3 km experiment, which result from the varying sizes of squall lines that are produced in this experiment but not in the experiments with parameterized convection (Movie S1).

These composites also show a striking difference between experiments: the organized precipitation systems are structurally different with resolved convection. While the composite rainfall rates exhibit a circular core in the 30 and 15 km experiments (Figures 14a and 14b), the 3 km experiment has sharper meridional rainfall gradients and a broader zonal extent (Figure 14c). For example, the 0.9 mm hr^{-1} contour of the composite extends beyond 2° east and west from the centroid of systems in the 3 km experiment, as compared to about 1.5° east and west from the centroid in the 30 and 15 km experiments. The meridional extent of the systems is also somewhat smaller at 3 km, extending up to 1.5° poleward and equatorward in contrast to 1.75° in the other experiments. Such contrasting structures point at different modes of convective organization; resolved deep convection produces more linear systems, whereas parameterized deep convection produces more circular clusters of convection.

This result is confirmed in Figure 12b through a distribution of the mathematical angle² between each system's axis and an east-west line. Only the 3 km experiment produces mostly zonally oriented precipitation systems; its distribution of angle is narrow and centered around zero. Precipitation systems in this experiment are mostly organized along east-west oriented rain bands. In contrast, the distributions from the experiments with

¹ System-relative fields of southern Hemisphere systems were flipped in latitude such that negative latitudes correspond to equatorward distance and positive latitudes correspond to poleward distance from the system centroid.

² To obtain the angle, MODE fits an ellipse to the points encompassing each system and then determines the orientation between the ellipse's major and minor axes. Figure S3 shows various examples of angles obtained from MODE.

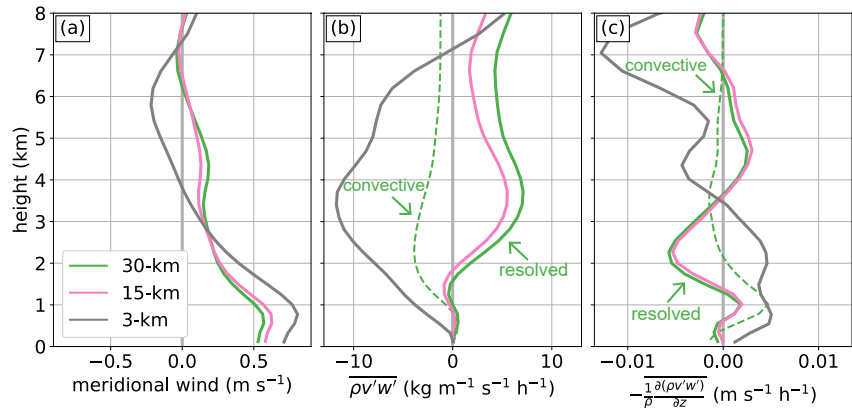


Figure 15. Composite vertical profiles of (a) meridional wind, (b) resolved vertical flux of meridional wind, and (c) vertical convergence of meridional wind flux averaged within 5° longitude and 2° latitude from the centroid of precipitation systems from the 30 (green), 15 (pink), and 3 km (grey) experiments. The dashed lines on panels (b) and (c) show the convective (i.e., parameterized) momentum flux and its convergence, respectively, from the 30 km experiment.

parameterized deep convection are broad and include more data points with absolute angles greater than zero. Such distribution implies that these experiments produce systems with a larger meridional extent or with a more southeast-northwest orientation than the 3 km experiment, which is consistent with the system-relative composites. Animated plots of rainfall rate confirm this finding and also show that the linear systems of the 3 km experiment propagate poleward (Movie S1).

Previous observational studies have shown that convective momentum transport depends on the orientation of tropical convective systems (LeMone et al., 1984; Moncrieff, 1992). In particular, linear systems have been associated with up-gradient (i.e., against the shear) upward momentum fluxes perpendicular to their propagation. To investigate if that is the case in our experiments, we obtained vertical profiles of meridional (v) winds and resolved convective momentum fluxes $\overline{v'w'}$, where the overbar represents zonal mean between -5° and 5° from the centroid of each system, the prime denotes a departure from that mean, and w is the vertical velocity). Figures 15a, 15b show those profiles averaged between 2° poleward and equatorward of the precipitation systems. We focus on the meridional wind, which is the component of the wind that is perpendicular to the dominant propagation of the organized systems in the aquaplanet experiments.

The meridional wind profile shows that the organized precipitation systems in the 3 km experiment are associated with stronger meridional shear between the middle and lower troposphere (850–500 hPa or 1–5 km; Figure 15a). Consistent with stronger shear, the 3 km experiment is associated with a different sign and vertical gradient of meridional momentum flux, with a peak negative value between 3 and 4 km (Figure 15b), such that the vertical convergence of the momentum flux yields a different sign of mean meridional wind tendency than the other experiments (Figure 15c). This means that the different momentum flux profile in the 3 km experiment acts to increase the shear in the lower and middle troposphere. Furthermore, since the meridional winds decrease with height, positive meridional momentum fluxes mean a up-gradient convective momentum transport in the 3 km experiment. In contrast, the other experiments have a down-gradient resolved-scale momentum transport that acts to weaken the meridional shear.

The convection parameterization also contributes to the total convective momentum flux. To examine this contribution, Figures 15b and 15c show the convective (i.e., parameterized) convective momentum flux and its vertical convergence only for the 30 km experiment. While the convective meridional momentum flux is negative, its vertical derivative shows that the largest contribution from this flux happens in the boundary layer below 2 km. The convective flux has a near-zero or negligible contribution above 2 km, where the resolved flux dominates. Even when accounting for these contributions, the total meridional momentum flux in the 30 and 15 km experiment acts to reduce the shear in the free troposphere. Although further analysis is needed, these results seem consistent with a lower frequency of linear systems when deep convection is mostly resolved.

The orientation of organized convective systems in the tropics depends, in part, on the strength and depth of cold pools (Grant et al., 2020). Indeed, another key difference between experiments is the coupling between

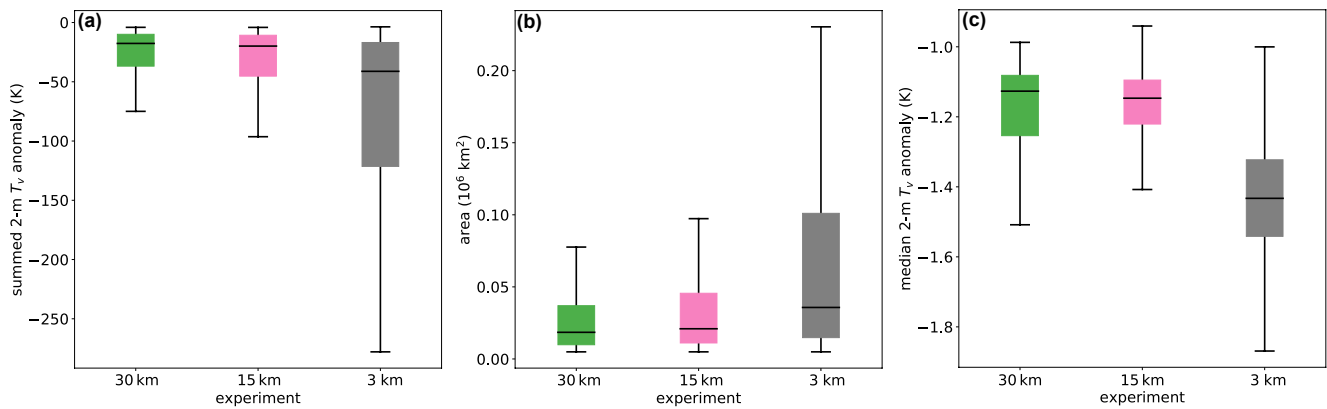


Figure 16. Box plots summarizing the distributions of (a) summed 2 m virtual temperature (T_v) anomaly, (b) total area of cold pools, and (c) median 2 m T_v anomaly from the (green) 30, (pink) 15, and (gray) 3 km experiments. Lines and boxes represent the same as in Figures 12 and 13.

rainfall and cold pools associated with the organized precipitation systems. Figures 14d–14f show system-relative composites of two metrics used to diagnose cold pools: 2-m virtual temperature anomaly (with respect to a zonal mean) and the magnitude of 10-m wind gradient—a recently introduced metric to identify cold pools from near-surface winds (Garg et al., 2020). Both metrics show a similar result: organized precipitation systems in the 3 km experiment are associated with stronger cold pools than in the experiments with parameterized deep convection. The strongest composite 2-m virtual temperature anomaly reaches approximately -0.4 K and the strongest 10-m wind gradient composite magnitude exceeds $3.0 \times 10^{-5} \text{ s}^{-1}$ in the 3 km experiment. In contrast, the strongest composite 2-m virtual temperature anomaly is approximately -0.2 K in both the 30 and 15 km experiments, and the strongest 10 m wind gradient is close to $1.5 \times 10^{-5} \text{ s}^{-1}$ in those experiments—a 50% reduction in cold pool strength per both metrics.

We recognize that the cold anomalies represented by the 2-m virtual temperature anomaly are not necessarily associated only with rainfall-induced cold pools. It is also possible that the cold anomalies stem from other synoptic-scale features that bring cool and dry boundary-layer air to the vicinity of precipitation systems. To confirm that the 3 km experiment produces stronger cold pools, we objectively identified cold pools using MODE. Here, system-scale cold pools are defined as three or more contiguous grid points (from the n256 interpolated analysis) bounded by the -1.0 K virtual temperature contour at 2-m height and with 50% or more overlap with an organized precipitation system as previously defined.

Using this methodology, we identified 390, 1,160, and 6,368 system-scale cold pools in the 30, 15, and 3 km experiments, respectively, over a 100 day period (Table 2). There are more than three times as many cold pools in the 3 km experiment than in the experiments with parameterized deep convection. Moreover, the distribution of cold pool intensity—as measured by the summed 2 m virtual temperature anomaly over the entire cold pool object—also shows that cold pools are much stronger in the 3 km experiment (Figure 16a). The 50th percentile of cold pool intensity is stronger (i.e., more negative) than the 25th percentile from the 30 to 15 km experiments. The stronger cold pools result from both larger cold pools as measured by the area of negatively 2-m virtual temperature anomaly (Figure 16b) and more negative buoyant air as depicted by the median intensity of each cold pool (Figure 16c). Both of those characteristics are likely a result of the parameterized rain evaporation. This analysis suggests that resolved deep convection results in a better coupling between rainfall and cold pools, such that heavier rainfall is associated with stronger, larger, and more numerous cold pools. Importantly, this result confirms the hypothesized relevance of cold pools in other simulations with resolved deep convection (Nasuno et al., 2007; Weber et al., 2020).

5. Discussion

Through a set of aquaplanet experiments using MPAS-A, we explored the effects of explicitly resolved deep convection on tropical rainfall and its multi-scale variability. Our findings are summarized through a schematic in Figure 17. All experiments using horizontal cell spacing of 15 km or greater, and thus having over 95% of rainfall contributed from a convection parameterization, showed a broad ITCZ and tropical rainfall variability

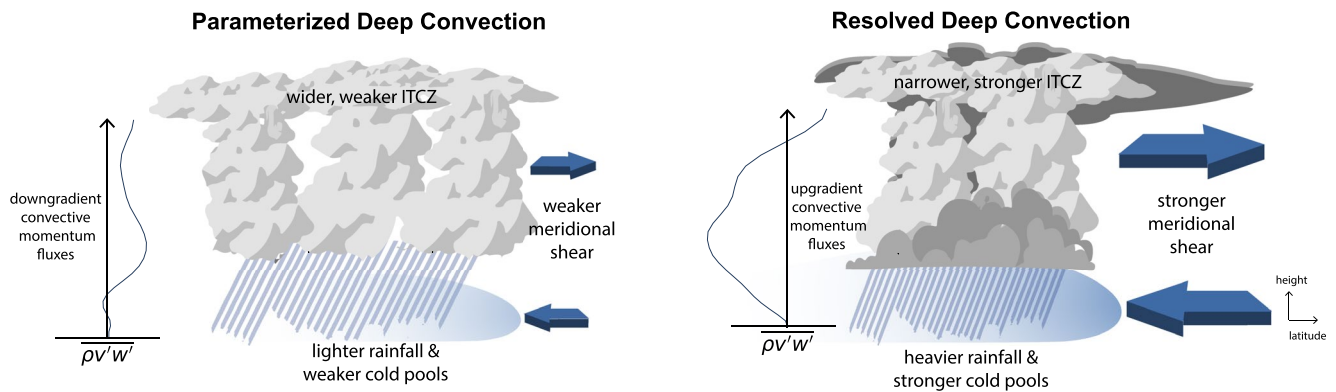


Figure 17. Summary schematic of tropical rainfall differences between the experiments with parameterized deep convection (left) and the experiment with resolved deep convection (right). The schematic represents a height-latitude cross section. Clouds and rainfall represent the intertropical convergence zone (ITCZ) and organized precipitation systems embedded within it. Blue arrows represent the zonally averaged, time-averaged meridional winds and the light blue shading represents cold pools. Lastly, convective momentum fluxes perpendicular to the ITCZ are shown with the thin blue lines.

predominantly driven by eastward propagating Kelvin waves. A novel experiment was presented with 3 km cell spacing and explicitly resolved deep convection in the tropics, which showed a narrower, more equatorward, and more intense ITCZ associated with stronger precipitation extremes. Furthermore, this 3 km experiment showed substantially larger tropical rainfall variance and more rainfall activity associated with short-lived and intense westward-propagating disturbances. An analysis of organized precipitation systems showed that a key difference between experiments was that the 3 km experiment produced linear systems with stronger and deeper cold pools, whereas the experiments with parameterized deep convection produced more circular clusters of convection.

The question remains as to how all these phenomena-specific differences relate to each other. We offer the following hypothesis to explain these differences (Figure 17): resolved deep convection results in a different feedback loop between the mean state, convective organization, and rainfall production. When deep convection is explicitly resolved, the mean state is associated with stronger meridional shear and a stronger meridional gradient of boundary-layer moist static energy. Those conditions favor convective organization in the form of linear systems, which are associated with up-gradient meridional convective momentum fluxes that act to reinforce the mean state vertical shear and lower-tropospheric meridional winds. At the same time, mechanical lifting within those linear systems contribute to heavy rainfall and strong cold pools, which act to support or even increase the meridional gradient of boundary-layer moist static energy and lower-tropospheric convergence. Those conditions support a narrower, more equatorward, and more intense ITCZ, and the feedback loop continues. In contrast, the different mean state conditions with parameterized deep convection support less linear convective clusters, down-gradient meridional convective momentum fluxes that weaken the mean state shear, weaker rainfall rates, and smoother meridional gradients that support a wider, more poleward, and weaker ITCZ. Those different feedback loops likely affect the equatorial waves as it has been recently shown that accurate representation of convective organization is critical to capture tropical rainfall variability (Chen et al., 2021; Moncrieff et al., 2017).

Our experiments have important implications for the representation of tropical rainfall, its organization and multi-scale variability in climate and weather prediction models. Tropical rainfall—from the mean state represented by the ITCZ to equatorial waves to rainfall extremes—is very similar amongst MPAS-A experiments with parameterized deep convection despite their different horizontal model resolutions. This result implies that the benefits of increasing horizontal resolution while parameterizing deep convection are minimal in comparison to the benefits of using convection-permitting resolution—at least for the convection parameterization and numerical model used here. While these results are based on a highly idealized configuration, a companion study finds similar results for a case study of a 40 day period simulated with cell spacing from 480 to 3.75 km (Judt & Rios-Berrios, 2021). More importantly, Judt and Rios-Berrios (2021) demonstrated that most of the differences when using a cell spacing under 10 km stemmed from the explicitly resolved convection—not from the smaller grid spacing. Together, Judt and Rios-Berrios (2021) and our study suggest that numerical simulations with sub-10-km grid spacing are a possible venue for improved weather predictions and climate projections of tropical rainfall and its multi-scale variability.

A potential shortcoming of our study is that we employed a scale-aware convection parameterization in the experiment with 3 km cell spacing in the tropics. Such parameterization was necessary because we used a variable resolution mesh with 15 km cell spacing outside the tropics. While over 90% of the tropical rainfall was explicitly resolved, the convective parameterization still contributed a small fraction of rainfall in that region. It is possible, although unproven, that the scale-aware convective parameterization mitigated some issues of global models with entirely resolved deep convection, such as the production of overly intense rainfall extremes or the lack of organized convective systems (e.g., Becker et al., 2021). This issue must be investigated to explore the possibility of using scale-aware convection parameterizations even when global models move to grid spacings smaller than 10 km (Freitas et al., 2020).

Data Availability Statement

Users interested in the post-processed model output examined in this manuscript should refer to the data set of Rios-Berrios et al. (2020a); Rios-Berrios et al. (2020b). Users who would like to produce their own output should access the MPAS-A source code with modifications for the aquaplanet configuration (Rios-Berrios, 2022).

Acknowledgments

Comments from Peter Bechtold, Andreas Prein, and two anonymous reviewers helped improve this manuscript. We are thankful to Simmi Sinha, Senior Designer at NCAR, for her help with the design of Figure 17. The authors acknowledge high-performance computing support from Cheyenne (<https://doi.org/10.5065/D6RX99HX>) provided by NCAR's Computational and Information Systems Laboratory. This material is based upon work supported by NCAR, which is a major facility sponsored by the National Science Foundation under Cooperative Agreement No. 1852977. Portions of this study were supported by the Regional and Global Model Analysis component of the Earth and Environmental System Modeling Program of the U.S. Department of Energy's Office of Biological & Environmental Research via National Science Foundation IA 1844590.

References

- Ahmed, F., Adames, Á. F., & Neelin, J. D. (2020). Deep convective adjustment of temperature and moisture. *Journal of the Atmospheric Sciences*, 77(6), 2163–2186. <https://doi.org/10.1175/JAS-D-19-0227.1>
- Ahmed, F., & Schumacher, C. (2017). Geographical differences in the tropical precipitation-moisture relationship and rain intensity onset. *Geophysical Research Letters*, 44(2), 1114–1122. <https://doi.org/10.1002/2016GL071980>
- Becker, T., Bechtold, P., & Sandu, I. (2021). Characteristics of convective precipitation over tropical Africa in storm-resolving global simulations. *The Quarterly Journal of the Royal Meteorological Society*, 147(741), 4388–4407. <https://doi.org/10.1002/qj.4185>
- Berry, G., & Reeder, M. J. (2014). Objective identification of the intertropical convergence zone: Climatology and trends from the ERA-interim. *Journal of Climate*, 27(5), 1894–1909. <https://doi.org/10.1175/JCLI-D-13-00339.1>
- Blackburn, M., & Hoskins, B. J. (2013). Context and aims of the aqua-planet experiment. *Journal of the Meteorological Society of Japan*, 91A, 1–15. <https://doi.org/10.2151/jmsj.2013-A01>
- Blackburn, M., Williamson, D. L., Nakajima, K., Ohfuchi, W., Takahashi, Y. O., Hayashi, Y.-Y., et al. (2013). The aqua-planet experiment (APE): CONTROL SST simulation. *Journal of the Meteorological Society of Japan*, 91A, 17–56. <https://doi.org/10.2151/jmsj.2013-A02>
- Bretherton, C. S., Peters, M. E., & Back, L. E. (2004). Relationships between water vapor path and precipitation over the tropical oceans. *Journal of Climate*, 17(2), 1517–1528. [https://doi.org/10.1175/1520-0442\(2004\)017<1517:RBWVPA>2.0.CO;2](https://doi.org/10.1175/1520-0442(2004)017<1517:RBWVPA>2.0.CO;2)
- Chen, C.-C., Richter, J. H., Liu, C., Moncrieff, M. W., Tang, Q., Lin, W., et al. (2021). Effects of organized convection parameterization on the MJO and precipitation in e3smv1. part I: Mesoscale heating. *Journal of Advances in Modeling Earth Systems*, 13(6), e2020MS002401. <https://doi.org/10.1029/2020MS002401>
- Davis, C. A., Brown, B. G., Bullock, R., & Halley-Gotway, J. (2009). The method for object-based diagnostic evaluation (MODE) applied to numerical forecasts from the 2005 NSSL/SPC spring program. *Weather and Forecasting*, 24(5), 1252–1267. <https://doi.org/10.1175/2009WAF2222241.1>
- Dias, J., Gehne, M., Kiladis, G. N., Sakaeda, N., Bechtold, P., & Haiden, T. (2018). Equatorial waves and the skill of NCEP and ECMWF numerical weather prediction systems. *Monthly Weather Review*, 146(6), 1763–1784. <https://doi.org/10.1175/MWR-D-17-0362.1>
- Freitas, S. R., Putman, W. M., Arnold, N. P., Adams, D. K., & Grell, G. A. (2020). Cascading toward a kilometer-scale GCM: Impacts of a scale-aware convection parameterization in the Goddard Earth observing system GCM. *Geophysical Research Letters*, 47(17), e2020GL087682. <https://doi.org/10.1029/2020GL087682>
- Frierson, D. M. W. (2007). Convectively coupled Kelvin waves in an idealized moist general circulation model. *Journal of the Atmospheric Sciences*, 64(6), 2076–2090. <https://doi.org/10.1175/JAS3945.1>
- Frierson, D. M. W., Kim, D., Kang, I.-S., Lee, M.-I., & Lin, J. (2011). Structure of AGCM-simulated convectively coupled Kelvin waves and sensitivity to convective parameterization. *Journal of the Atmospheric Sciences*, 68(1), 26–45. <https://doi.org/10.1175/2010JAS3356.1>
- Garg, P., Nesbitt, S. W., Lang, T. J., Pritts, G., Chronis, T., Thayer, J. D., & Hence, D. A. (2020). Identifying and characterizing tropical oceanic mesoscale cold pools using spaceborne scatterometer winds. *Journal of Geophysical Research: Atmospheres*, 125, e2019JD031812. <https://doi.org/10.1029/2019JD031812>
- Gonzalez, A. O., & Schubert, W. H. (2019). Violation of Ekman balance in the Eastern Pacific ITCZ boundary layer. *Journal of the Atmospheric Sciences*, 76(9), 2919–2940. <https://doi.org/10.1175/JAS-D-18-0291.1>
- Grant, L. D., Moncrieff, M. W., Lane, T. P., & van den Heever, S. C. (2020). Shear-parallel tropical convective systems: Importance of cold pools and wind shear. *Geophysical Research Letters*, 47(12), e2020GL087720. <https://doi.org/10.1029/2020GL087720>
- Haiden, T., Rodwell, M. J., Richardson, D. S., Okagaki, A., Robinson, T., & Hewson, T. (2012). Intercomparison of global model precipitation forecast skill in 2010/11 using the SEEPS score. *Monthly Weather Review*, 140(8), 2720–2733. <https://doi.org/10.1175/MWR-D-11-00301.1>
- Hohenegger, C., Kornbluh, L., Klocke, D., Becker, T., Cioni, G., Engels, J. F., et al. (2020). Climate statistics in global simulations of the atmosphere, from 80 to 2.5 km grid spacing. *Journal of the Meteorological Society of Japan*, 98(1), 73–91. <https://doi.org/10.2151/jmsj.2020-005>
- Hong, S.-Y., Dudhia, J., & Chen, S.-H. (2004). A revised approach to ice microphysical processes for the bulk parameterization of clouds and precipitation. *Monthly Weather Review*, 132, 103–120. [https://doi.org/10.1175/1520-0493\(2004\)132<0103:ARATIM>2.0.CO;2](https://doi.org/10.1175/1520-0493(2004)132<0103:ARATIM>2.0.CO;2)
- Hong, S.-Y., Noh, Y., & Dudhia, J. (2006). A new vertical diffusion package with an explicit treatment of entrainment processes. *Monthly Weather Review*, 134(9), 2318–2341. <https://doi.org/10.1175/MWR3199.1>
- Houze, R. A., Jr. (2004). Mesoscale convective systems. *Reviews of Geophysics*, 42(4), RG4003. <https://doi.org/10.1029/2004RG000150>
- Iacono, M. J., Delamere, J. S., Mlawer, E. J., Shephard, M. W., Clough, S. A., & Collins, W. D. (2008). Radiative forcing by long-lived greenhouse gases: Calculations with the AER radiative transfer models. *Journal of Geophysical Research*, 113, D13103. <https://doi.org/10.1029/2008JD009944>

- Judt, F. (2018). Insights into atmospheric predictability through global convection-permitting model simulations. *Journal of the Atmospheric Sciences*, 75(5), 1477–1497. <https://doi.org/10.1175/JAS-D-17-0343.1>
- Judt, F., Klocke, D., Rios-Berrios, R., Vanniere, B., Ziemer, F., Auger, L., et al. (2021). Tropical cyclones in global storm-resolving models. *Journal of the Meteorological Society of Japan*, 99(3), 579–602. <https://doi.org/10.2151/jmsj.2021-029>
- Judt, F., & Rios-Berrios, R. (2021). Resolved convection improves the representation of equatorial waves and tropical rainfall variability in a global nonhydrostatic model. *Geophysical Research Letters*, 48(14), e2021GL093265. <https://doi.org/10.1029/2021GL093265>
- Kiladis, G. N., Wheeler, M. C., Haertel, P. T., Straub, K. H., & Roundy, P. E. (2009). Convectively coupled equatorial waves. *Reviews of Geophysics*, 47(2), RG2003. <https://doi.org/10.1029/2008RG000266>
- LeMone, M. A., Barnes, G. M., & Zipser, E. J. (1984). Momentum flux by lines of cumulonimbus over the tropical oceans. *Journal of the Atmospheric Sciences*, 41(2), 1914–1932. [https://doi.org/10.1175/1520-0469\(1984\)041<1914:MFBLOC>2.0.CO;2](https://doi.org/10.1175/1520-0469(1984)041<1914:MFBLOC>2.0.CO;2)
- Lin, J.-L. (2007). The double-ITCZ problem in IPCC ar4 coupled GCMS: Ocean–atmosphere feedback analysis. *Journal of Climate*, 20(18), 4497–4525. <https://doi.org/10.1175/jcli4272.1>
- Lin, J.-L., Kiladis, G. N., Mapes, B. E., Weickmann, K. M., Sperber, K. R., Lin, W., et al. (2006). Tropical intraseasonal variability in 14 IPCC AR4 climate models. Part I: Convective signals. *Journal of Climate*, 19(12), 2665–2690. <https://doi.org/10.1175/JCLI3735.1>
- Liu, Y., Guo, L., Wu, G., & Wang, Z. (2010). Sensitivity of ITCZ configuration to cumulus convective parameterizations on an aqua planet. *Climate Dynamics*, 34(2–3), 223–240. <https://doi.org/10.1007/s00382-009-0652-2>
- Mapes, B., Tulich, S., Lin, J., & Zuidema, P. (2006). The mesoscale convection life cycle: Building block or prototype for large-scale tropical waves? *Dynamics of Atmospheres and Oceans*, 42(1–4), 3–29. <https://doi.org/10.1016/j.dynatmoce.2006.03.003>
- Mechoso, C. R., Robertson, A. W., Barth, N., Davey, M. K., Delecluse, P., Gent, P. R., et al. (1995). The seasonal cycle over the tropical Pacific in coupled ocean-atmosphere general circulation models. *Monthly Weather Review*, 123(9), 2825–2838. [https://doi.org/10.1175/1520-0493\(1995\)123<2825:tscott>2.0.co;2](https://doi.org/10.1175/1520-0493(1995)123<2825:tscott>2.0.co;2)
- Möbis, B., & Stevens, B. (2012). Factors controlling the position of the intertropical convergence zone on an aquaplanet. *Journal of Advances in Modeling Earth Systems*, 4(4), M00A04. <https://doi.org/10.1029/2012MS000199>
- Moncrieff, M. W. (1992). Organized convective systems: Archetypal dynamical models, mass and momentum flux theory, and parametrization. *The Quarterly Journal of the Royal Meteorological Society*, 118(507), 819–850. <https://doi.org/10.1002/qj.49711850703>
- Moncrieff, M. W., Liu, C., & Bogenschutz, P. (2017). Simulation, modeling, and dynamically based parameterization of organized tropical convection for global climate models. *Journal of the Atmospheric Sciences*, 74(5), 1363–1380. <https://doi.org/10.1175/JAS-D-16-0166.1>
- Nakajima, K., Yamada, Y., Takahashi, Y. O., Ishiwatari, M., Ohfuchi, W., & Hayashi, Y.-Y. (2013). The variety of spontaneously generated tropical precipitation patterns found in APE results. *Journal of the Meteorological Society of Japan*, 91A(0), 91–141. <https://doi.org/10.2151/jmsj.2013-A04>
- Nasuno, T., Tomita, H., Iga, S., Miura, H., & Satoh, M. (2007). Multiscale organization of convection simulated with explicit cloud processes on an aquaplanet. *Journal of the Atmospheric Sciences*, 64(6), 1902–1921. <https://doi.org/10.1175/JAS3948.1>
- Neale, R., & Hoskins, B. J. (2001). A standard test for AGCMs including their physical parametrizations: I: The proposal. *Atmospheric Science Letters*, 1(2), 101–107. <https://doi.org/10.1006/asle.2000.0019>
- Neelin, J. D., Peters, O., & Hales, K. (2009). The transition to strong convection. *Journal of the Atmospheric Sciences*, 66(8), 2367–2384. <https://doi.org/10.1175/2009JAS2962.1>
- Nesbitt, S. W., Cifelli, R., & Rutledge, S. A. (2006). Storm morphology and rainfall characteristics of TRMM precipitation features. *Monthly Weather Review*, 134(10), 2702–2721. <https://doi.org/10.1175/MWR3200.1>
- Nolan, D. S., Tulich, S. N., & Blanco, J. E. (2016). ITCZ structure as determined by parameterized versus explicit convection in aquachannel and aquapatch simulations. *Journal of Advances in Modeling Earth Systems*, 8(1), 425–452. <https://doi.org/10.1002/2015MS000560>
- Pearson, K. J., Lister, G. M. S., Birch, C. E., Allan, R. P., Hogan, R. J., & Woolnough, S. J. (2014). Modelling the diurnal cycle of tropical convection across the ‘grey zone’: Modelling the diurnal cycle of tropical convection. *Quarterly Journal of the Royal Meteorological Society*, 140(679), 491–499. <https://doi.org/10.1002/qj.2145>
- Peatman, S. C., Methven, J., & Woolnough, S. J. (2018). Isolating the effects of moisture entrainment on convectively coupled equatorial waves in an aquaplanet GCM. *Journal of the Atmospheric Sciences*, 75(9), 3139–3157. <https://doi.org/10.1175/JAS-D-18-0098.1>
- Prein, A. F., Liu, C., Ikeda, K., Trier, S. B., Rasmussen, R. M., Holland, G. J., & Clark, M. P. (2017). Increased rainfall volume from future convective storms in the US. *Nature Climate Change*, 7(12), 880–884. <https://doi.org/10.1038/s41558-017-0007-7>
- Retsch, M. H., Mauritsen, T., & Hohenegger, C. (2019). Climate change feedbacks in aquaplanet experiments with explicit and parametrized convection for horizontal resolutions of 2,525 up to 5 km. *Journal of Advances in Modeling Earth Systems*, 11(7), 2070–2088. <https://doi.org/10.1029/2019MS001677>
- Rios-Berrios, R. (2022). *Mpas-a v6.2 with modifications to use the aquaplanet capability*. Zenodo. Retrieved from <https://doi.org/10.5281/zenodo.6323189>
- Rios-Berrios, R., Medeiros, B., & Bryan, G. H. (2020a). *Aquaplanet simulations using the model for prediction across scales (MPAS) version 6.2*. NCAR/UCAR - GDEX. Retrieved from <https://doi.org/10.5065/cam1-v353>
- Rios-Berrios, R., Medeiros, B., & Bryan, G. H. (2020b). Mean climate and tropical rainfall variability in aquaplanet simulations using the model for prediction across scales – atmosphere. *Journal of Advances in Modeling Earth Systems*, 12(10). <https://doi.org/10.1029/2020MS002102>
- Seo, K.-H., Choi, J.-H., & Han, S.-D. (2012). Factors for the simulation of convectively coupled Kelvin waves. *Journal of Climate*, 25(10), 3495–3514. <https://doi.org/10.1175/JCLI-D-11-00060.1>
- Skamarock, W. C., Klemp, J. B., Duda, M. G., Fowler, L. D., Park, S.-H., & Ringler, T. D. (2012). A multiscale nonhydrostatic atmospheric model using centroidal Voronoi tessellations and C-grid staggering. *Monthly Weather Review*, 140(9), 3090–3105. <https://doi.org/10.1175/MWR-D-11-00215.1>
- Stephens, G. L., L’Ecuyer, T., Forbes, R., Gettelman, A., Golaz, J.-C., Bodas-Salcedo, A., et al. (2010). Dreary state of precipitation in global models. *Journal of Geophysical Research*, 115, D24211. <https://doi.org/10.1029/2010jd014532>
- Stevens, B., Satoh, M., Auger, L., Biercamp, J., Bretherton, C. S., Chen, X., et al. (2019). DYAMOND: The DYNAMics of the atmospheric general circulation modeled on non-hydrostatic domains. *Progress in Earth and Planetary Science*, 6(1), 61. <https://doi.org/10.1186/s40645-019-0304-z>
- Straub, K. H., Haertel, P. T., & Kiladis, G. N. (2010). An analysis of convectively coupled Kelvin waves in 20 WCRP CMIP3 global coupled climate models. *Journal of Climate*, 23(11), 3031–3056. <https://doi.org/10.1175/2009JCLI3422.1>
- Tomita, H. (2005). A global cloud-resolving simulation: Preliminary results from an aqua planet experiment. *Geophysical Research Letters*, 32(8), L08805. <https://doi.org/10.1029/2005GL022459>
- Trenberth, K. E., & Zhang, Y. (2018). How often does it really rain? *Bulletin of the American Meteorological Society*, 99(2), 289–298. <https://doi.org/10.1175/BAMS-D-17-0107.1>

- Vogel, P., Knippertz, P., Fink, A. H., Schlueter, A., & Gneiting, T. (2018). Skill of global raw and postprocessed ensemble predictions of rainfall over Northern tropical Africa. *Weather and Forecasting*, *33*(2), 369–388. <https://doi.org/10.1175/WAF-D-17-0127.1>
- Wang, W. (2022). Forecasting convection with a 'scale-aware' tiedtke cumulus parameterization scheme at kilometer scales. *Weather and Forecasting*.
- Weber, N. J., & Mass, C. F. (2019). Subseasonal weather prediction in a global convection-permitting model. *Bulletin of the American Meteorological Society*, *100*(6), 1079–1089. <https://doi.org/10.1175/BAMS-D-18-0210.1>
- Weber, N. J., Mass, C. F., & Kim, D. (2020). The impacts of horizontal grid spacing and cumulus parameterization on subseasonal prediction in a global convection-permitting model. *Monthly Weather Review*, *148*(12), 4747–4765. <https://doi.org/10.1175/MWR-D-20-0171.1>
- Wedi, N. P., Polichtchouk, I., Dueben, P., Anantharaj, V. G., Bauer, P., Boussetta, S., et al. (2020). A baseline for global weather and climate simulations at 1 km resolution. *Journal of Advances in Modeling Earth Systems*, *12*(11), e2020MS002192. <https://doi.org/10.1029/2020ms002192>
- Wheeler, M., & Weickmann, K. M. (2001). Real-time monitoring and prediction of modes of coherent synoptic to intraseasonal tropical variability. *Monthly Weather Review*, *129*(12), 2677–2694. [https://doi.org/10.1175/1520-0493\(2001\)129<2677:RTMAPO>2.0.CO;2](https://doi.org/10.1175/1520-0493(2001)129<2677:RTMAPO>2.0.CO;2)
- Williamson, D. L., Blackburn, M., Nakajima, K., Ohfuchi, W., Takahashi, Y. O., Hayashi, Y.-Y., et al. (2013). The aqua-planet experiment (ape): Response to changed meridional SST profile. *Journal of the Meteorological Society of Japan*, *91A*, 57–89. <https://doi.org/10.2151/jmsj.2013-A03>
- Xu, K.-M., & Randall, D. A. (1996). A semiempirical cloudiness parameterization for use in climate models. *Journal of the Atmospheric Sciences*, *53*(2), 3084–3102. [https://doi.org/10.1175/1520-0469\(1996\)053<3084:ASCPFU>2.0.CO;2](https://doi.org/10.1175/1520-0469(1996)053<3084:ASCPFU>2.0.CO;2)
- Yuter, S. E., & Houze, R. A. (1995). Three-dimensional kinematic and microphysical evolution of Florida cumulonimbus. Part III: Vertical mass transport, mass divergence, and synthesis. *Monthly Weather Review*, *123*, 1964–1983. [https://doi.org/10.1175/1520-0493\(1995\)123<1964:TDKAME>2.0.CO;2](https://doi.org/10.1175/1520-0493(1995)123<1964:TDKAME>2.0.CO;2)
- Zhang, C., & Wang, Y. (2017). Projected future changes of tropical cyclone activity over the Western North and South Pacific in a 20-km-Mesh regional climate model. *Journal of Climate*, *30*(15), 5923–5941. <https://doi.org/10.1175/JCLI-D-16-0597.1>
- Zipser, E. J., & LeMone, M. A. (1980). Cumulonimbus vertical velocity events in GATE. Part II: Synthesis and model core structure. *Journal of the Atmospheric Sciences*, *37*, 2458–2469. [https://doi.org/10.1175/1520-0469\(1980\)037<2458:CVVEIG>2.0.CO;2](https://doi.org/10.1175/1520-0469(1980)037<2458:CVVEIG>2.0.CO;2)